RIM-BP2 regulates Ca^{2+} channel clustering and neurotransmitter release at hippocampal mossy fiber terminals.

Rinako Miyano[1], Hirokazu Sakamoto[2], Kenzo Hirose[2, 3], and Takeshi Sakaba[1]

[1]Graduate School of Brain Science, Doshisha University, Kyotanabe-shi, Kyoto 610-0394, Japan

[2]Department of Pharmacology, Graduate School of Medicine, The University of Tokyo, Bunkyo-ku, Tokyo 113-0033, Japan

[3]International Research Center for Neurointelligence (WPI-IRCN), The University of Tokyo, Bunkyo-ku, Tokyo 113-0033, Japan

Abstract

Synaptic vesicles dock and fuse at the presynaptic active zone (AZ), the specialized site for transmitter release. AZ proteins play multiple roles such as recruitment of Ca^{2+} channels as well as synaptic vesicle docking, priming and fusion. However, the precise role of each AZ protein type remains unknown. At phasic synapses having high release probability, Rab3-interacting molecule-binding protein2 (RIM-BP2) is known to affect Ca^{2+} channel localization at AZs. In order to dissect the role of RIM-BP2 at tonic synapses having low

release probability, we applied electrophysiological recording and super-resolution imaging to hippocampal mossy fiber terminals of RIM-BP2 KO mice. By using direct presynaptic recording, we found the reduced Ca^{2+} currents. The measurements of EPSCs and presynaptic capacitance suggested that the initial release probability was lowered because of the reduced Ca^{2+} influx and impaired fusion competence in RIM-BP2 KO. Nevertheless, larger Ca^{2+} influx restored release. Consistent with presynaptic recording, STED microscopy suggested lower densities of P/Q-type Ca^{2+} channels at AZs deficient in RIM-BP2. Our results suggest that the RIM-BP2 function differs between phasic and tonic synapses.

Introduction

At chemical synapses, an action potential arriving at the presynaptic terminal opens voltage-gated Ca^{2+} channels, and Ca^{2+} influx through voltage-gated Ca^{2+} channels triggers neurotransmitter release from synaptic vesicles within a millisecond. Synaptic vesicle fusion occurs at a specialized region of the presynaptic membrane called the active zone (AZ), where Ca^{2+} channel clusters and vesicle fusion sites are accommodated via AZ scaffold proteins (Südhof, 2012). For rapid transmission, accumulation of Ca^{2+} channels, co-localization of Ca^{2+} channels and fusion sites, and molecular priming of synaptic vesicles for fusion are required, and the differences between these factors might provide a basis for

37 synaptic diversity. However, it remains unknown how these factors are regulated by AZ-
38 scaffold proteins.

39 Rab3-interacting molecule-binding proteins (RIM-BPs) represent one principal,
40 conserved family of AZ proteins and bind to RIMs and Ca^{2+} channels (Wang et al., 2000;
41 Hibino et al., 2002). RIM-BP family includes RIM-BP1, RIM-BP2, and RIM-BP3 in mammals,
42 but RIM-BP3 expression is low in the nervous system (Mittelstaedt and Schoch, 2007). In
43 *Drosophila* neuromuscular junctions (NMJs), loss of RIM-BPs decreases Ca^{2+} channel
44 density and reduces release probability (Liu et al., 2011). Moreover, RIM-BP in *Drosophila*
45 NMJs is necessary for tight coupling of synaptic vesicles to Ca^{2+} channels and replenishment
46 of high release probability vesicles at *Drosophila* NMJs (Liu et al., 2011; Müller et al., 2015,
47 Petzoldt et al., 2020). In mammalian synapses, the observations from KO mice are diverse.
48 In RIM-BP1,2 DKO mice, the coupling between Ca^{2+} channels and synaptic vesicles became
49 loose, and action potential-evoked neurotransmitter release was reduced at the calyx of Held
50 synapse (Acuna et al., 2015). At hippocampal CA3-CA1 synapses, RIM-BP2 deletion alters
51 Ca^{2+} channel localization at the AZs without altering total Ca^{2+} influx. Besides, RIM-BP1,2
52 DKO has no additional effect, indicating that RIM-BP2 dominates the function of RIM-BP
53 isoforms (Grauel et al., 2016). Tight coupling between Ca^{2+} channels and vesicles is crucial
54 for rapid and efficient transmitter release (Wadel et al., 2007).

55 In contrast, hippocampal mossy fiber-CA3 synapses are characterized by low
56 release probability (Vyleta and Jonas, 2014). At hippocampal mossy fiber synapses, gSTED
57 imaging suggested that RIM-BP2 KO altered the Munc13-1 cluster number and distribution.
58 In addition, RIM-BP2 deletion decreased the number of docked vesicles (Brockmann et al.,
59 2019). However, because of technically difficulty, direct and quantitative measurements of
60 exocytosis in RIM-BP2 KO terminals have not been performed so far.

61 To quantify the RIM-BP2 function in mossy fiber-CA3 synapses, we performed
62 whole-cell patch-clamp recordings from WT and RIM-BP2 KO hippocampal mossy fiber
63 boutons. From electrophysiological recordings, we show that the reductions of Ca^{2+} current
64 amplitudes in RIM-BP2 KO terminals. The EPSC and capacitance measurements suggest
65 that the reduction of Ca^{2+} currents is responsible, in part, for that of transmitter release. In
66 addition, they suggest that fusion competence is impaired, which can be overcome by larger
67 Ca^{2+} influx into the terminal. Using STED imaging, we find the densities of P/Q-type Ca^{2+}
68 channels in terminals to be reduced in RIM-BP2 KO. We suggest that RIM-BP2 regulates the
69 number of P/Q-type Ca^{2+} channels at the AZ and is critical for transmitter release at
70 hippocampal mossy fiber terminals.

71

72 **Results**

73 **RIM-BP2 KO reduces presynaptic calcium currents at hippocampal mossy fiber**
74 **boutons.**

75 To investigate the roles of RIM-BP2 in synaptic transmission, we examined the
76 kinetics of exocytosis and Ca^{2+} influx in WT and RIM-BP2 KO synapses using presynaptic
77 whole-cell capacitance measurements (Fig. 1). When the terminal was depolarized from -80
78 mV to +10 mV for 10 ms, Ca^{2+} currents and membrane capacitance were recorded as shown
79 in Fig. 1A. During the depolarizing pulse, capacitance was not measured due to large
80 conductance changes, and the increase was used for measuring synaptic vesicle exocytosis.
81 To determine the size of the RRP and the time course of exocytosis, we measured
82 capacitance changes (ΔC_m) in response to various durations of depolarization. Here, the
83 length of the depolarizing pulse was varied between 5 ms and 100 ms, and ΔC_m was plotted
84 against pulse duration (Fig. 1B and Figure 1-figure supplement 1, bottom). ΔC_m became
85 larger as the duration of pulse was prolonged, but the increase started to be saturated at a
86 100 ms pulse in WT terminals, suggesting depletion of the RRP. ΔC_m in response to a 100
87 ms pulse was 52 ± 8.1 fF (n = 9, Fig. 1B). The amplitude corresponds to the fusion of about
88 500-600 synaptic vesicles (Hallermann et al., 2003; Midorikawa and Sakaba, 2017). The time
89 course of ΔC_m could be fitted by a single exponential with a time constant of 59 ± 12 ms. In
90 RIM-BP2 KO terminals, ΔC_m in response to a 100 ms pulse was somewhat smaller (41 ± 5.9

91 fF, n = 8) than that of WT terminals, and the release time constant was somewhat slower (64
92 ± 14 ms) than in WT terminals. We should note that the time constant is not necessarily
93 reliable because the ΔC_m values do not reach a plateau value at 100 ms pulse in some
94 terminals. Although the capacitance jumps of KO may be smaller for shorter pulses,
95 capacitance measurements are not sensitive enough to detect small changes (< 5 fF, 50
96 vesicles, see Fig. 5 & Fig. 6). Nevertheless, the differences in the time course of capacitance
97 were not significantly different between WT and KO ($p = 0.23$ from ANOVA) and the effects
98 on release examined by strong pulses depleting the RRP was relatively minor. The
99 amplitudes of Ca^{2+} currents were smaller in RIM-BP2 KO terminals as compared to WT
100 terminals (Fig. 1B and Figure 1-figure supplement 1, top, $p < 0.05$ from ANOVA). The Ca^{2+}
101 current in response to a 100 ms pulse was reduced by ~30% in RIM-BP2 KO terminals (27
102 ± 3.9 pA, n = 8) compared to WT terminals (44 ± 5.4 pA, n = 9) ($p = 0.0248$, t-test, Fig. 1B).
103 Thus, the results show that RIM-BP2 deletion reduces presynaptic Ca^{2+} influx, but effects on
104 the RRP size and the time course of release measured by capacitance measurements are
105 relatively minor.

106 To investigate the Ca^{2+} influx in more detail, we examined the voltage dependence
107 of Ca^{2+} currents. Fig. 1C shows voltage step protocols and representative current traces. In
108 both genotypes, Ca^{2+} currents started to be activated at around -20 mV, and maximal

amplitude was observed at ~+10 mV (Fig. 1D). There was no major difference in the voltage dependence of Ca^{2+} currents between WT and RIM-BP2 KO mice. Consistently, activation time constants of Ca^{2+} currents were similar between WT and RIM-BP2 KO, when the terminal was depolarized to +10 mV (τ = 1.4 ± 0.2 ms in WT, n = 6; τ = 1.3 ± 0.2 ms in KO, n = 4). These results suggest a reduction in the number of Ca^{2+} channels rather than changes in activation kinetics is responsible for the current decrease observed.

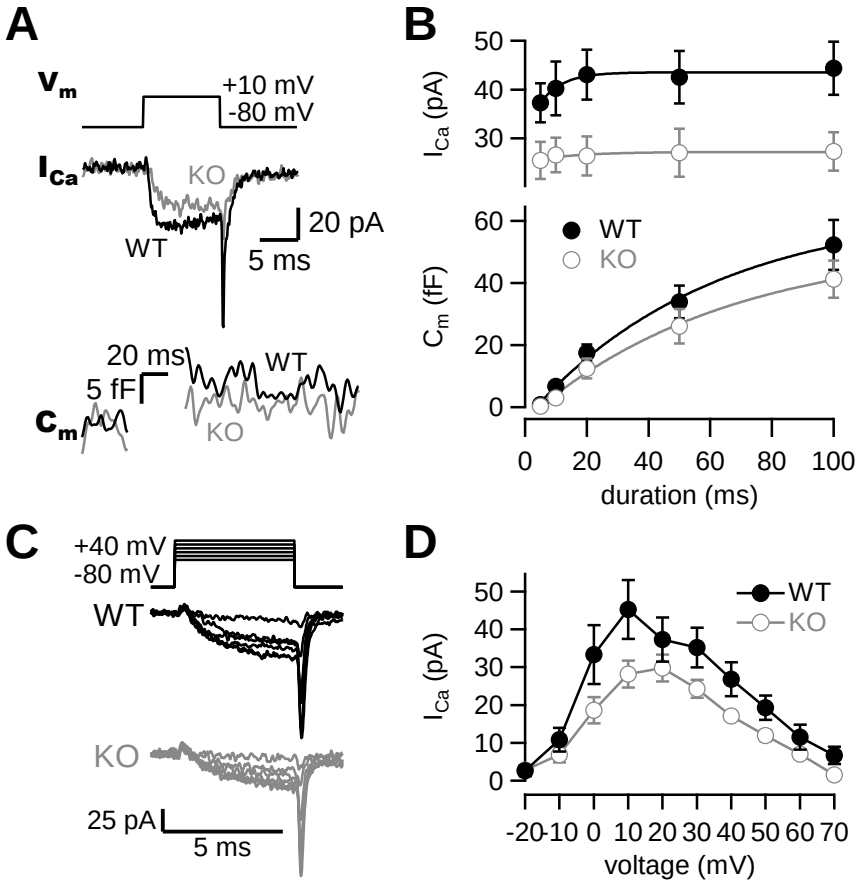

Figure 1. Presynaptic calcium currents and synaptic vesicle release in RIM-BP2 KO mice

(**A**) The terminal was depolarized from -80 mV to +10 mV in WT (black) and RIM-BP2 KO (gray) hippocampal mossy fiber boutons. Ca^{2+} currents (I_{Ca}) and membrane capacitance (C_m) in response to a 10 ms pulse (V_m) are shown. (**B**) *(top)* The peak Ca^{2+} currents were plotted against the pulse duration. WT vs KO, $p = 0.034$ (ANOVA). *(bottom)* The capacitance jumps were plotted against the pulse duration. WT vs KO, $p = 0.23$ (ANOVA). Black filled circles and gray open circles represent the data from WT (n = 9 from 8 animals) and RIM-BP2 KO (n = 8 from 6 animals), respectively. Each data point represents mean ± SEM. (**C**) Experimental protocol and representative traces for presynaptic Ca^{2+} current measurements in WT (black) and RIM-BP2 KO (gray) boutons. Terminals were sequentially depolarized for 5 ms with 2 ms intervals from -80 mV to +70 mV by 10 mV steps. (**D**) Current-voltage relationships of peak Ca^{2+} currents in WT (black filled circle; n = 4-6 from 4 animals) and RIM-BP2 KO (gray open circle; n = 4-5 from 5 animals). I_{Ca}s were elicited by 5 ms depolarizations. Two curves are significantly different ($p < 0.01$ from mixed model). Each data point represents mean ± SEM. Numerical values of plots are provided in Figure 1-source data 1.

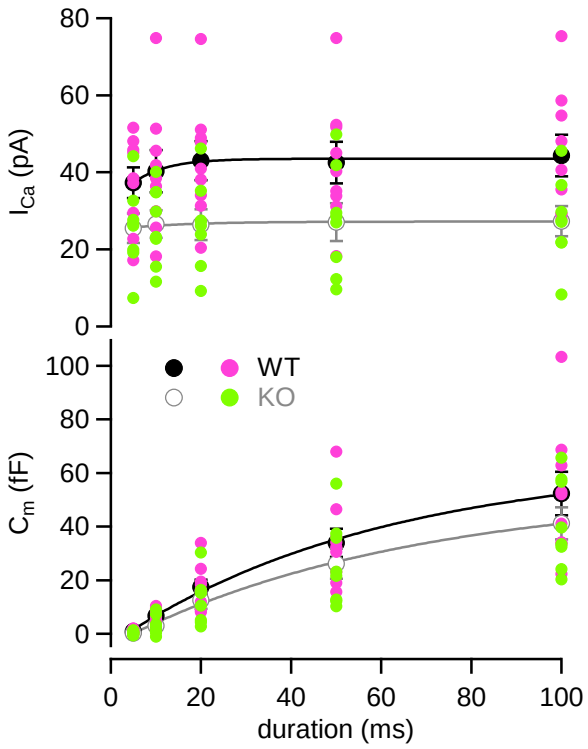

Figure 1-figure supplement 1. Individual value plot of Fig. 1B

Individual values of I_{Ca}s (*top*) and C_ms (*bottom*) in WT (pink) and RIM-BP2 KO (green) terminals were plotted against the pulse duration. Numerical values of plots are provided in Figure 1-source data 1.

Figure 1-source data 1. Datasets of Ca^{2+}-current and capacitance amplitudes presented in Figure 1 and Figure 1-figure supplement 1.

The effects of extracellular calcium concentration on Ca^{2+} influx and capacitance changes in WT and RIM-BP2 KO.

Because Ca^{2+} currents were reduced in RIM-BP2 KO mice, we tested whether the

145 reduction of Ca^{2+} currents could be restored by elevation of the external Ca^{2+} concentration.

146 We raised the extracellular Ca^{2+} concentration ($[Ca^{2+}]_{ext}$) from 2 mM to 4 mM (Fig. 2). Ca^{2+}

147 currents and membrane capacitances were recorded at 4 mM $[Ca^{2+}]_{ext}$, and amplitudes then

148 plotted against pulse duration (Fig. 2A and Figure 2-figure supplement 1). Although Ca^{2+}

149 current elicited by a 100 ms pulse in RIM-BP2 KO was still smaller (33 ± 2.7 pA, n = 3) than

150 that in WT (54 ± 6.1 pA, n = 6) (Fig. 2B, top) in 4 mM Ca^{2+}, Ca^{2+} currents of KO mice at 4

151 mM $[Ca^{2+}]_{ext}$ were comparable to those of WT at 2 mM $[Ca^{2+}]_{ext}$.

152 At 4 mM $[Ca^{2+}]_{ext}$, ΔC_m in response to a 100 ms pulse in RIM-BP2 KO was 51 ± 11

153 fF (n = 3) and showed a similar value in WT at 2 mM $[Ca^{2+}]_{ext}$ (Fig. 2B, bottom). At the same

154 time, ΔC_m in WT was not altered (52 ± 2.5 fF, n = 6) at higher $[Ca^{2+}]_{ext}$. The time course of

155 exocytosis at 4 mM $[Ca^{2+}]_{ext}$ in KO was similar to that of WT at 2 mM $[Ca^{2+}]_{ext}$, as the time

156 courses were superimposable in Fig. 2A (p = 0.57 from mixed model).

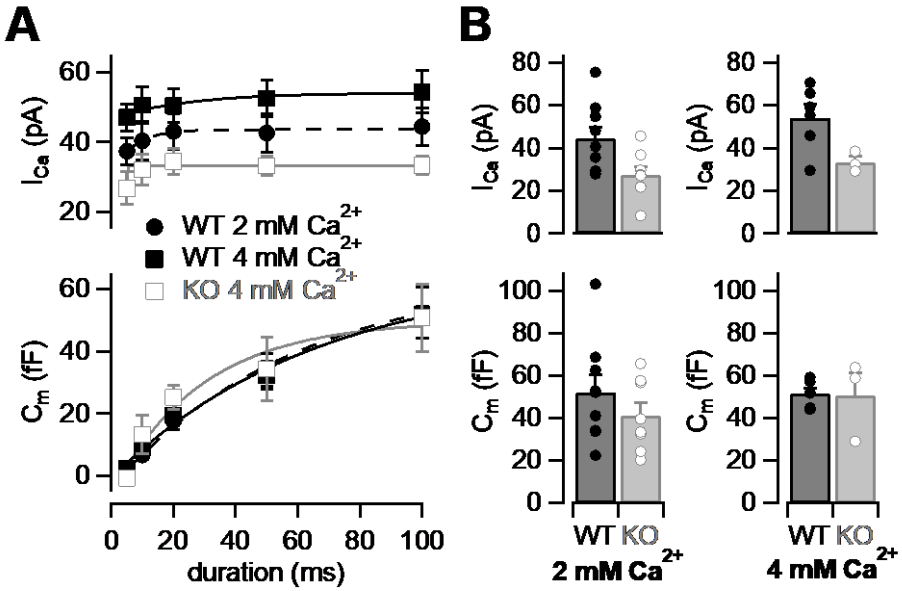

157

158 **Figure 2. The effects of high extracellular calcium concentration on Ca^{2+} currents and**

159 **capacitance changes.**

160 (**A**) The I_{Ca}s (*top*) and the C_ms (*bottom*) are plotted against the pulse duration. Black filled

161 squares and gray open squares represent the data from WT (n = 6-8 from 6 animals) and

162 RIM-BP2 KO (n = 3-4 from 2 animals) at 4 mM $[Ca^{2+}]_{ext}$, respectively. For comparison, the

163 WT data in 2 mM $[Ca^{2+}]_{ext}$ are superimposed (black filled circle; n = 9) (the same data set as

164 Fig. 1B). Each data point represents mean ± SEM. I_{Ca}s were significantly different between

165 WT and KO in 4 mM $[Ca^{2+}]_{ext}$ ($p < 0.01$ from mixed model). The WT I_{Ca}s in 2 mM $[Ca^{2+}]_{ext}$ and

166 the KO I_{Ca}s in 4 mM $[Ca^{2+}]_{ext}$ were significantly different ($p < 0.02$ from mixed model), but Cm

167 were not significantly different ($p = 0.57$ from mixed model). (**B**) Average I_{Ca}s *(top)* and C_ms

168 *(bottom)* in response to a 100 ms pulse in WT (black bars) and RIM-BP2 KO (gray bars)

169 terminals. Extracellular Ca^{2+} concentration was 2 mM *(left)* or 4 mM *(right)*. Error bars show

SEM. Circles indicate individual values. Numerical values of plots are provided in Figure 2-source data 1.

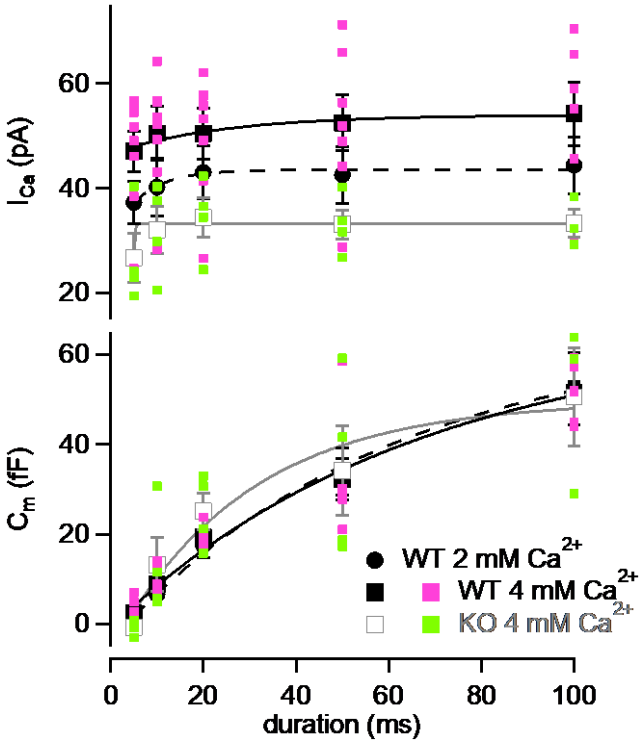

Figure 2-figure supplement 1. Individual value plot of Fig. 2A

Individual values of I_{Ca}s (*top*) and C_ms (*bottom*) recorded at 4 mM $[Ca^{2+}]_{ext}$ in WT (pink) and RIM-BP2 KO (green) terminals are plotted against the pulse duration. Numerical values of plots are provided in Figure 2-source data 1.

Figure 2-source data 1. Datasets of Ca^{2+}-current and capacitance amplitudes presented in Figure 2 and Figure 2-figure supplement 1.

181 Next, we adjusted Ca^{2+} current amplitudes of WT to that of RIM-BP2 KO by lowering

182 $[Ca^{2+}]_{ext}$ (Fig. 3). The amplitudes of Ca^{2+} currents and capacitance jumps were plotted against

183 pulse duration (Fig. 3A and Figure 3-figure supplement 1). At 1 mM $[Ca^{2+}]_{ext}$, Ca^{2+} currents

184 and ΔC_m were smaller than those of RIM-BP2 KO at 2 mM $[Ca^{2+}]_{ext}$. At 1.5 mM $[Ca^{2+}]_{ext}$, Ca^{2+}

185 currents became more comparable to those of RIM-BP2 KO at 2 mM $[Ca^{2+}]_{ext}$ ($p = 0.12$ from

186 mixed model). Here, the ΔC_m evoked by a 100 ms pulse (43 ± 6.7 fF, n = 5) was comparable

187 between WT and RIM-BP2 KO (Fig. 3A). The average time course of capacitance increase

188 of WT at 1.5 mM $[Ca^{2+}]_{ext}$ was similar to that of RIM-BP2 KO at 2 mM $[Ca^{2+}]_{ext}$ ($p = 0.88$ from

189 mixed model). Therefore, by reducing Ca^{2+} currents, WT data could reproduce similar release

190 time course of RIM-BP2 KO. In Fig. 3B, ΔC_m in response to a 100 ms pulse at various

191 $[Ca^{2+}]_{ext}$s were plotted against the peak Ca^{2+} current amplitudes. The relationship could be

192 fitted by a Hill plot with n = 3 in WT (Schneggenburger et al., 1999). Consistently, when

193 capacitance jumps elicited by various pulse durations are plotted against total Ca^{2+} influx

194 (Figure 3-figure supplement 2), the RIM-BP2 KO data were superimposed on the WT data.

195 In Fig. 3C, relative amplitudes of Ca^{2+} currents and capacitance in response to a 100 ms

196 pulse are plotted. The RIM-BP2 KO data were superimposed on the WT data, suggesting

197 that the RRP size were similar between WT and KO (~50 fF). Taken together, presynaptic

198 capacitance measurements were not able to detect differences in the release rates between

199 WT and KO especially when Ca^{2+} influx in WT and KO was adjusted to be similar. In particular,

200 the RRP sizes measured by the pool depleting stimulation were not altered strongly by RIM-

201 BP2 KO. The results may mean that RIM-BP2 is dispensable for transmitter release or that

202 large Ca^{2+} influx may overcome the deficit of the release. Alternatively, capacitance

203 measurements may not be sensitive enough to detect the differences between WT and KO

204 at short stimulation, which are relevant for AP-evoked release (see below, Fig. 5 and Fig. 6).

205

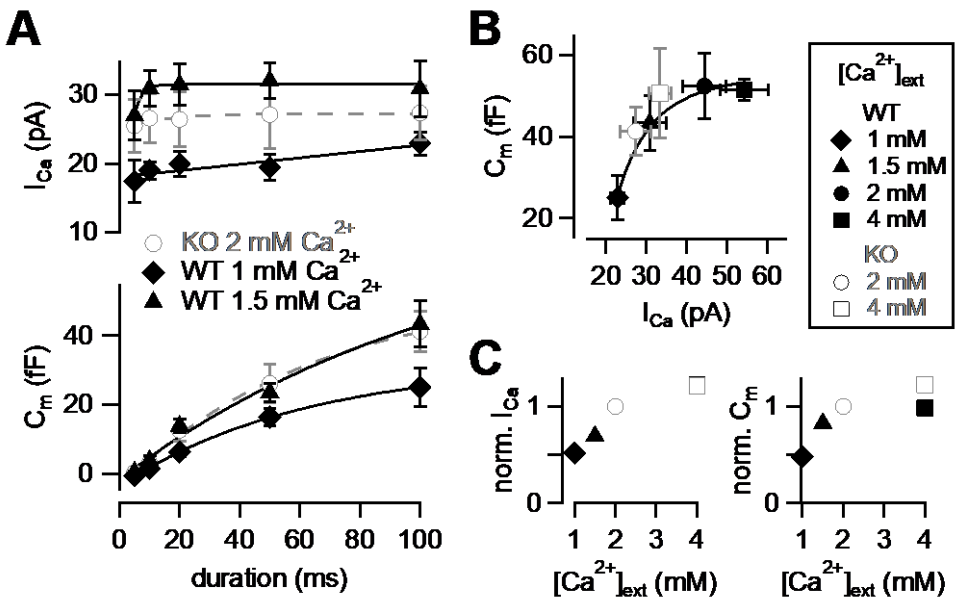

206

207 **Figure 3. Calcium-dependence of the release kinetics and the RRP size**

208 (**A**) *(top)* The relationship between peak Ca^{2+} currents and pulse durations at different

209 $[Ca^{2+}]_{ext}$s. *(bottom)* The relationship between capacitance jumps and pulse durations at

210 different $[Ca^{2+}]_{ext}$s. Gray open circles, black diamonds and black triangles represent the data

211 from RIM-BP2 KO at 2 mM $[Ca^{2+}]_{ext}$ (n = 8) (the same data set as Fig. 1B), WT at 1 mM

212 $[Ca^{2+}]_{ext}$ (n = 3-5 from 4 animals) and WT at 1.5 mM $[Ca^{2+}]_{ext}$ (n = 5-7 from 6 animals),

213 respectively. Each data point represents mean ± SEM. (**B**) Capacitance jumps at various

214 $[Ca^{2+}]_{ext}$s are plotted against calcium current amplitudes. Pulses were 100 ms depolarization

215 from -80 mV to +10 mV. Each data point represents mean ± SEM. Data points were fitted

216 with a Hill equation with n = 3. (**C**) *(left)* Average I_{Ca}s at indicated $[Ca^{2+}]_{ext}$s were normalized

217 to the response at 2 mM $[Ca^{2+}]_{ext}$ in each genotype. *(right)* Average C_ms at indicated $[Ca^{2+}]_{ext}$s

218 were normalized to the 2 mM $[Ca^{2+}]_{ext}$ response in each genotype. Numerical values of plots

219 are provided in Figure 3-source data 1.

220

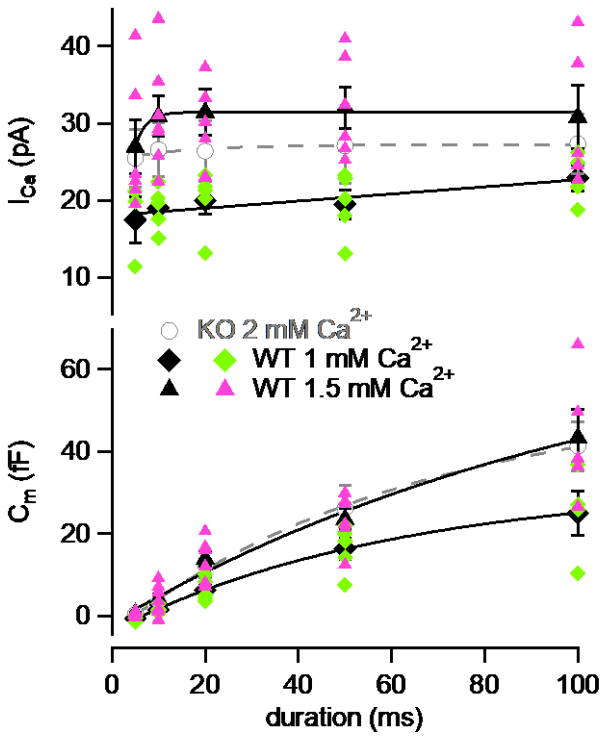

221

222 **Figure 3-figure supplement 1. Individual value plot of Fig. 3A**

Individual values of I_{Ca}s (*top*) and C_ms (*bottom*) recorded at 1 mM (green) or 1.5 mM (pink) $[Ca^{2+}]_{ext}$ in WT were plotted against the pulse duration. Numerical values of plots are provided in Figure 3-source data 1.

Figure 3-source data 1. Datasets of numerical values presented in Figure 3 and Figure 3-figure supplement 1,

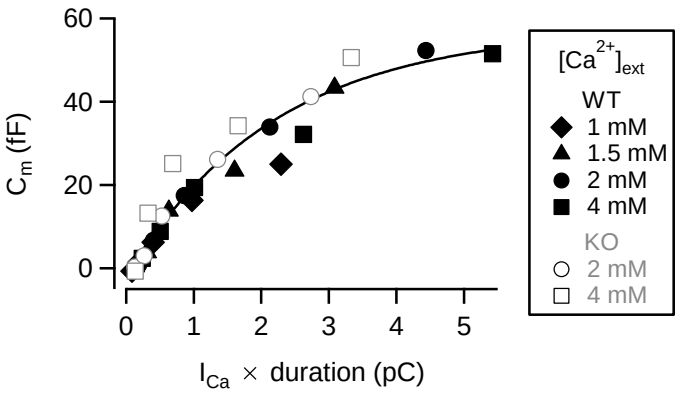

Figure 3-figure supplement 2. The relationship between synaptic vesicle release and total Ca^{2+} charge

Capacitance jumps elicited by various pulse durations are plotted against total Ca^{2+} charge. The total Ca^{2+} charge is calculated by multiplying a peak Ca^{2+} current amplitude by pulse duration. Each symbol represents a data point obtained from WT (black filled symbols) and RIM-BP2 KO (gray open symbols) mice at various $[Ca^{2+}]_{ext}$. Data points were fitted by a single exponential function. Numerical values of plots are provided in Figure 3-figure supplement 2-source data 1.

238 **Figure 3-figure supplement 2-source data 1.** Datasets of Ca^{2+} charge and ΔC_m presented

239 in Figure 3-figure supplement 2.

240

241 **High EGTA experiments suggest unaltered coupling between calcium channels and**

242 **synaptic vesicles.**

243 Previous studies have used Ca^{2+} chelator such as EGTA to examine the sensitivity

244 of release to intracellular Ca^{2+} buffers (Adler et al., 1991; Borst & Sakmann, 1996; Vyleta &

245 Jonas, 2014). When the physical coupling between Ca^{2+} channels and synaptic vesicles is

246 tight, EGTA (slow Ca^{2+} chelator) has less effect on release probability, but EGTA is effective

247 when the coupling is loose. Previous experiments have suggested that RIM-BPs regulate the

248 channel-vesicle coupling at the calyx of Held (Acuna et al., 2015). If this observation also

249 applies to the mossy fiber synapse, EGTA sensitivity of release should be higher in RIM-BP2

250 KO terminals. To investigate the coupling at mossy fiber boutons in RIM-BP2 KO, we

251 changed the concentration of EGTA in the patch pipette. In the presence of 5 mM EGTA, we

252 depolarized the terminal from -80 mV to +10 mV for 5 ms and recorded Ca^{2+} currents and

253 membrane capacitance (Fig. 4A). Ca^{2+} currents and ΔC_m were plotted against pulse duration

254 (Fig. 4B and Figure 4-figure supplement 1). In both WT and RIM-BP2 KO mice, ΔC_m were

255 reduced under 5 mM EGTA compared with the control condition of 0.5 mM EGTA. We

256 compared the effect of EGTA on average amplitudes of peak Ca^{2+} currents in response to a
257 20 ms pulse (Fig. 4D). Interestingly, Ca^{2+} current amplitudes were ~1.2 times larger at 5 mM
258 EGTA (53 ± 12 pA, n = 5) than at 0.5 mM EGTA (43 ± 5.1 pA, n = 9) in WT, though the data
259 scattered under 5 mM EGTA condition and there was no statistically significant difference (p
260 = 0.36, t-test). In RIM-BP2 KO, we did not observe such an increase. EGTA might inhibit Ca^{2+}
261 channel inactivation in WT (von Gersdorff and Matthews, 1996). In Fig. 4C, we compared the
262 effect of EGTA on the ΔC_m in response to a 20 ms pulse. In both genotypes, ΔC_m values
263 were inhibited by 5 mM EGTA, and the inhibition was larger in RIM-BP2 KO (EGTA
264 inhibition: $p < 0.01$, genotypes $p > 0.05$ from mixed model).

265 Ca^{2+} current amplitudes in RIM-B2 KO are smaller than in WT (Fig. 4B). It is possible
266 that strong effect of high EGTA on release maybe due to reduced Ca^{2+} currents in RIM-BP2
267 KO. Therefore, we changed $[Ca^{2+}]_{ext}$ from 2 mM to 1 mM and adjusted Ca^{2+} current
268 amplitudes of WT to the RIM-BP2 KO level. The capacitance increase and the amplitudes of
269 Ca^{2+} currents became similar to those of RIM-BP2 KO (Fig. 4C and Fig. 4D). These results
270 indicate that WT and RIM-BP2 KO terminals have similar sensitivity of neurotransmitter
271 release to EGTA. Thus, it is unlikely that changes in the coupling distance are responsible
272 for the reduced exocytosis of the mutants.

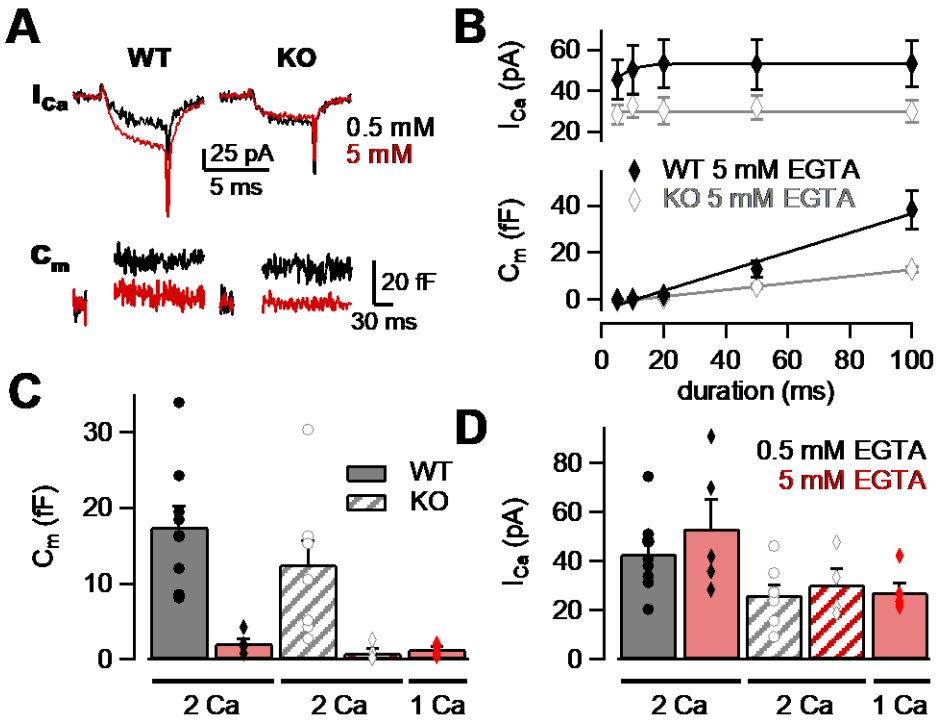

Figure 4. The effects of high EGTA on calcium currents and synaptic vesicle exocytosis

(**A**) Example traces in response to a 5 ms depolarizing pulse to +10 mV in WT *(left)* and RIM-BP2 KO *(right)* boutons. Ca^{2+} current (I_{Ca}) and membrane capacitance (C_m) recorded with 0.5 mM EGTA (black) or 5 mM EGTA (red) in the patch pipette are shown. (**B**) The I_{Ca}s *(top)* and C_ms *(bottom)* are plotted against the pulse duration. The patch pipette contained 5 mM EGTA. Black filled diamonds and gray open diamonds represent the data from WT (n = 4-5 from 4 animals) and RIM-BP2 KO (n = 4 from 3 animals), respectively. Each data point indicates mean ± SEM. (**C, D**) Average C_ms (**C**) and I_{Ca}s (**D**) elicited by a 20 ms pulse in WT (filled bars) and RIM-BP2 KO (hatched bars). The extracellular Ca^{2+} concentration was 1 mM

(from 5 animals) or 2 mM. The intracellular solution contained either 0.5 mM EGTA (black) or 5 mM EGTA (red). Error bars show SEM. Circles and diamonds indicate individual values. Numerical values of plots are provided in Figure 4-source data 1.

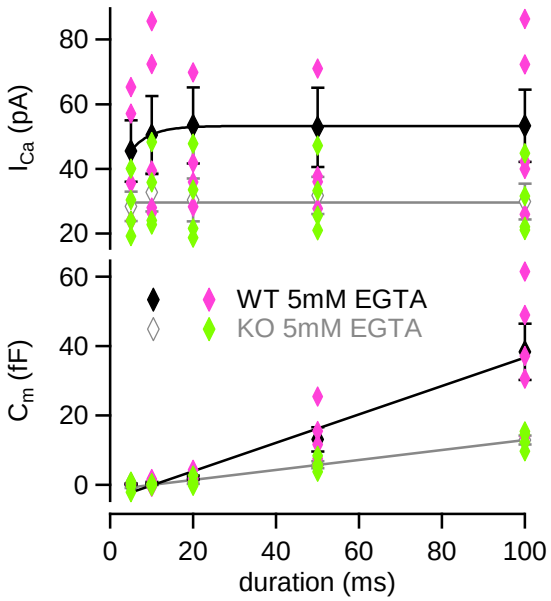

Figure 4-figure supplement 1. Individual value plot of Fig. 4B

Individual values of I_{Ca}s (*top*) and C_ms (*bottom*) recorded in the presence of 5 mM EGTA in WT (green) and KO (pink) were plotted against the pulse duration. Numerical values of plots are provided in Figure 4-source data 1.

Figure 4-source data 1. Datasets of Ca^{2+}-current and capacitance amplitudes presented in Figure 4 and Figure 4-figure supplement 1.

Smaller AP-evoked EPSCs in KO could not be explained entirely by the reduced Ca^{2+}

297 **influx.**

298 While Ca^{2+} current amplitudes were clearly reduced in KO, capacitance jumps were
299 reduced little. Capacitance measurements could only detect large amounts of exocytosis (~5
300 fF, 50 vesicles), and the changes relevant for the AP-evoked release (< 10 vesicles per AP
301 per synapse) could not be detected. Moreover, large Ca^{2+} influx used for the stimulation
302 protocol of Fig.1 to Fig. 3 could overcome the deficits of RIM-BP2 KO. In order to detect the
303 changes related to physiological conditions, we measured the AMPA-EPSCs evoked by
304 electrical mossy fiber stimulation at CA3 pyramidal cells (Fig. 5). As seen in Fig. 5A, the
305 EPSCs were evoked by dual stimulation of mossy fibers. The mossy-fiber evoked responses
306 were confirmed by the relatively faster EPSC kinetics and sensitivity to DCG-Ⅳ (1 μM), a
307 mGluR2 agonist (remaining response of < 30 %, 0.23 ± 0.01 for WT (n = 5), 0.29 ± 0.02 for
308 KO (n = 5)). Because multiple fibers were stimulated, we could not estimate the number of
309 vesicles released per one synapse. Nevertheless, when fibers were stimulated similarly, the
310 EPSC amplitudes of KO were much smaller (893 ± 202 pA in WT, n = 7; 189 ± 73 pA in KO,
311 n = 7) (p = 0.011). In Fig. 2, presynaptic recordings indicated that Ca^{2+} current amplitudes of
312 KO at 4 mM $[Ca^{2+}]_{ext}$ became similar to those of WT at 2 mM $[Ca^{2+}]_{ext}$ (Fig. 2). The EPSCs
313 became larger when the $[Ca^{2+}]_{ext}$ was raised from 2 mM to 4 mM in KO (Fig. 5A, bottom, see
314 also Figure 6-figure supplement 1) and became more similar to those of WT. In Fig. 3,

315 presynaptic recording showed that I_{Ca}s of WT at 1.5 mM $[Ca^{2+}]_{ext}$ were similar to those of KO
316 at 2 mM $[Ca^{2+}]_{ext}$. However, the WT EPSCs at 1.5 mM $[Ca^{2+}]_{ext}$ seemed larger than KO at 2
317 mM $[Ca^{2+}]_{ext}$ (Fig. 5A, top, see also Figure 6-figure supplement 1). Changing the $[Ca^{2+}]_{ext}$
318 from 1.5 mM to 2 mM in WT and from 2 mM to 4 mM in KO should have the same potentiation
319 effect on the EPSCs, if the reduced Ca^{2+} current amplitudes are the only mechanism for
320 reduced EPSCs in KO. In Fig. 5B, we calculated two types of potentiation ratios: In WT, the
321 ratio of the EPSC response in 2 mM to that in 1.5 mM $[Ca^{2+}]_{ext}$ was calculated in each cell.
322 In KO, the ratio of the EPSC response in 4 mM to that in 2 mM $[Ca^{2+}]_{ext}$ was calculated in
323 each cell. When these two values were compared, the ratios were much larger in KO (Fig.
324 5B, $p < 0.01$, t-test). Release probability is more sensitive to the $[Ca^{2+}]_{ext}$ in the low end of
325 the dose-response curve because of the 3rd-4th power dependence of release on $[Ca^{2+}]_{ext}$ at
326 the low end (Dodge and Rahamimoff, 1967; Schneggenburger and Neher, 2000; Bollmann
327 et al., 2000). Therefore, the result suggests lower release probability in KO, even when the
328 amounts of Ca^{2+} influx were adjusted to be similar. When the paired pulse ratios were
329 compared, all four conditions (WT in 1.5 mM and 2 mM $[Ca^{2+}]_{ext}$, KO in 2 mM and 4 mM
330 $[Ca^{2+}]_{ext}$) provided similar values (Fig. 5C). The paired pulse ratio should be inversely
331 correlated to release probability, in principle. However, paired pulse facilitation in mossy fiber
332 synapses could be mediated by multiple factors, including Ca^{2+}-independent broadening of

333 AP waveforms (Geiger and Jonas, 2000) and Ca^{2+} buffer saturation which is more
334 pronounced and increases the paired-pulse ratios at higher $[Ca^{2+}]_{ext}$ (Blatow et al., 2003).
335 Therefore, the value might not be sensitive to the $[Ca^{2+}]_{ext}$.

336 We also analyzed the EPSCs in response to a stimulus train (50 Hz × 25 or 26
337 pulses) both in WT and KO (Fig. 6) under different external Ca^{2+} concentrations. When the
338 WT and KO responses were compared, the time course of facilitation/depression was quite
339 different between WT and KO (Fig. 6A-Fig. 6C). In 2 mM $[Ca^{2+}]_{ext}$, WT responses showed
340 initial facilitation (~2 fold) followed by depression, whereas KO responses showed
341 pronounced facilitation of ~10 fold. The difference could be due to both reduced Ca^{2+} currents
342 and impaired fusion competence in KO.

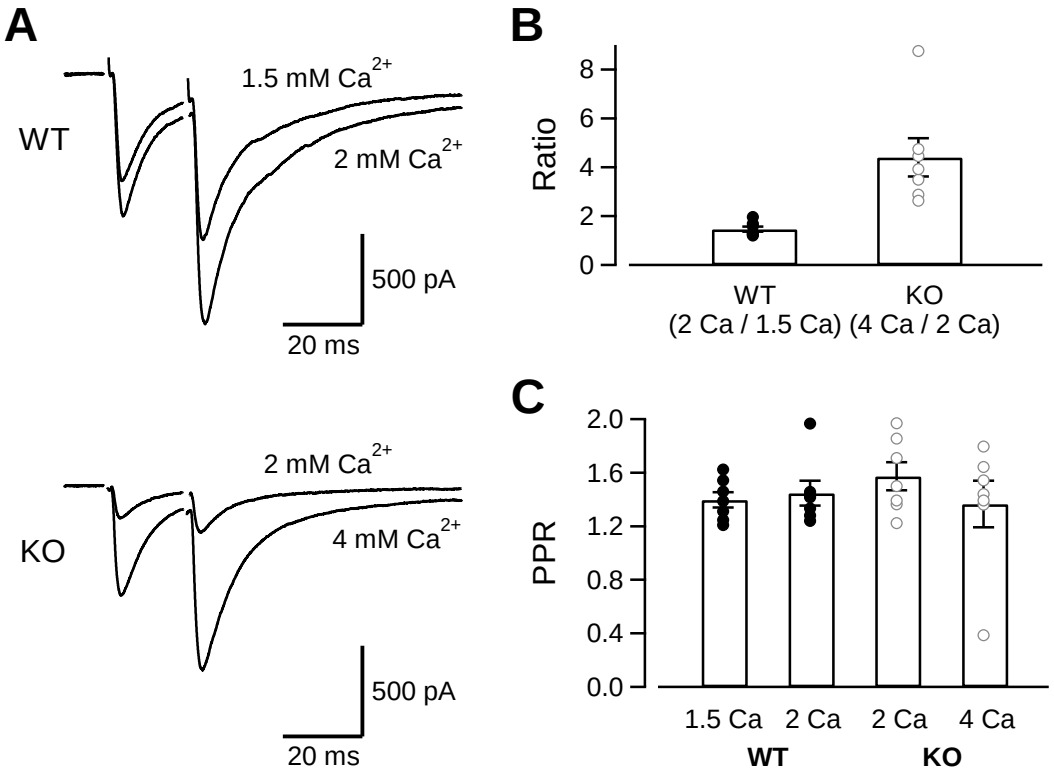

Figure 5. The evoked EPSC amplitudes in WT and KO, and their sensitivity to the extracellular Ca^{2+}

(**A**) The mossy fiber-evoked EPSCs measured at CA3 pyramidal cells. The fibers were stimulated twice with an interval of 20 ms. The responses of WT in 1.5 mM and 2 mM $[Ca^{2+}]_{ext}$ (n = 7 cells from 5 animals), as well as those of KO in 2 mM and 4 mM $[Ca^{2+}]_{ext}$ (n = 7 cells from 6 animals) are shown. The stimulus artifacts were blanked. (**B**) The amplitude ratios of WT EPSCs (2 mM / 1.5 mM $[Ca^{2+}]_{ext}$) and KO EPSCs (4 mM / 2 mM $[Ca^{2+}]_{ext}$) are shown. The concentrations were chosen to set the Ca^{2+} influx similar between WT and KO from Fig. 1-Fig. 3. (**C**) The paired pulse ratios under 4 conditions (WT in 1.5 mM and 2 mM $[Ca^{2+}]_{ext}$, KO in 2 mM and 4 mM $[Ca^{2+}]_{ext}$). Numerical values of plots are provided in Figure 5-source

data 1.

Figure 5-source data 1. Datasets of numerical values presented in Figure 5.

To adjust presynaptic Ca^{2+} influx to the similar level as the KO terminals, the $[Ca^{2+}]_{ext}$ was reduced to 1.5 mM in WT. Under this condition, presynaptic Ca^{2+} current amplitudes were expected to be similar between WT and KO (in 2 mM $[Ca^{2+}]_{ext}$). If the reduced Ca^{2+} influx is only responsible for smaller EPSCs in KO, we will observe similar time course of train responses between WT and KO. However, facilitation was much less in the WT condition (at 1.5 mM $[Ca^{2+}]_{ext}$, Fig. 6D, $p < 0.05$ from ANOVA), suggesting the mechanism independent of Ca^{2+} influx. In order to obtain the same Ca^{2+} influx as that of WT in 2 mM $[Ca^{2+}]_{ext}$, the $[Ca^{2+}]_{ext}$ was increased to 4 mM in KO. The time course of facilitation was somewhat larger in the KO condition compared with that WT in 2 mM $[Ca^{2+}]_{ext}$. Because of the data scatter in KO, the time course was statistically not significant ($p > 0.05$ from ANOVA). Because multiple fibers were stimulated, the absolute EPSC amplitudes depend on not only the release probability and the number of release sites per synapse, but also the number of stimulated synapses. Nevertheless, when the absolute amplitudes were plotted against the stimulus number, the differences were most prominent at the first responses in the train and the differences were diminished later in the train, suggesting that the initial release probability

372 is likely to be lower at RIM-BP2 KO synapses, but the release could be restored during

373 repetitive stimulation (Figure 6-figure supplement 1). Restoration of release is consistent with

374 minor difference of capacitance changes in response to the depolarization (Figs. 1-4).

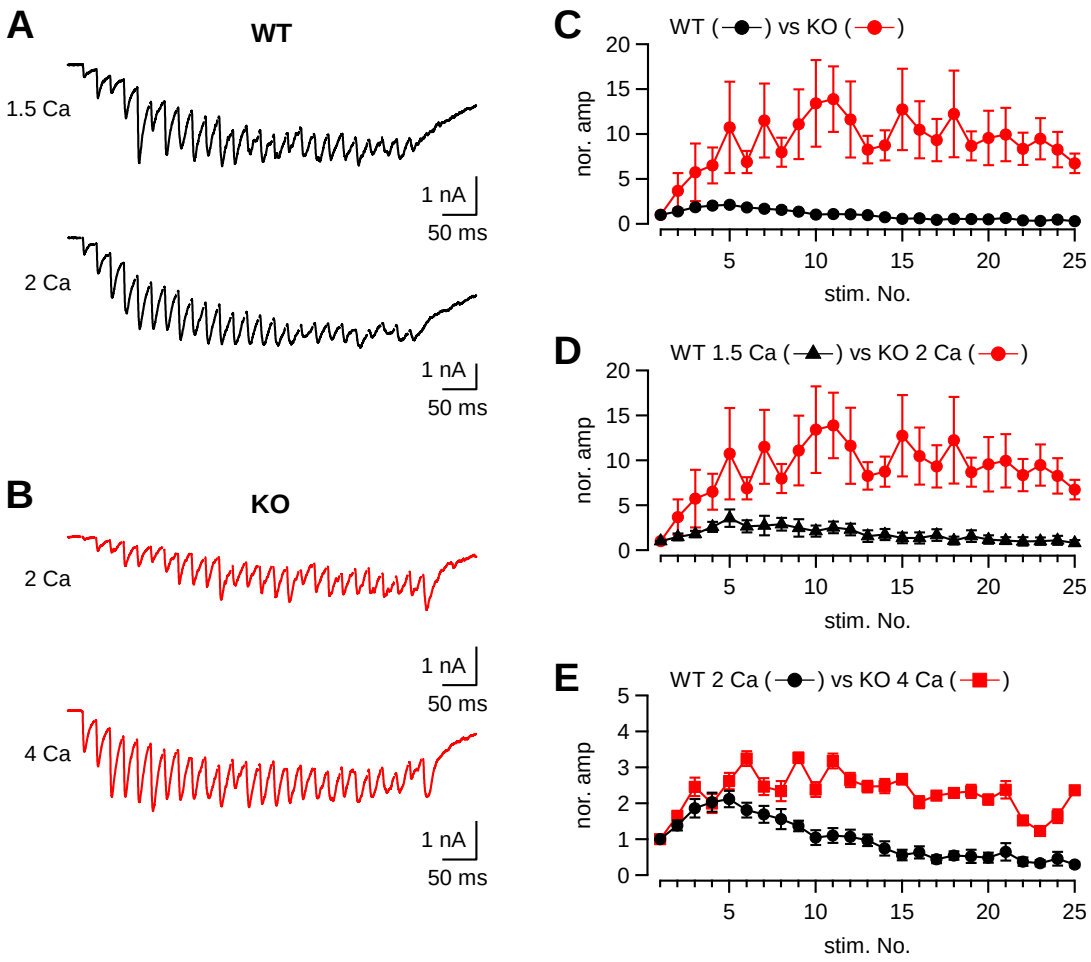

375

376 **Figure 6. The time course of synaptic facilitation/depression in WT and KO**

377 (**A**) Mossy fibers were stimulated at 50 Hz (25 times) and the evoked EPSCs were measured

378 in 1.5 mM (n = 5 cells from 4 animals) and 2 mM $[Ca^{2+}]_{ext}$ (n = 7 cells from 5 animals) in WT.

379 The stimulus artifacts were blanked. (**B**) Mossy fibers were stimulated at 50 Hz (26 times in

380 this particular example), and the evoked EPSCs were measured in 2 mM (n = 7 cells from 6

animals) and 4 mM $[Ca^{2+}]_{ext}$ (n = 8 cells from 6 animals). (**C**) The time course of EPSC amplitudes during a 50 Hz train. The data were obtained from WT and KO in 2 mM $[Ca^{2+}]_{ext}$. The time courses were significantly different ($p < 0.01$ from ANOVA). (**D**) The same as (**C**), but the data were obtained from WT in 1.5 mM $[Ca^{2+}]_{ext}$ and KO in 2 mM $[Ca^{2+}]_{ext}$. The time courses were significantly different ($p < 0.05$ from ANOVA). (**E**) The same as (**C**), but the data were obtained from WT in 2 mM $[Ca^{2+}]_{ext}$ and KO in 4 mM $[Ca^{2+}]_{ext}$. Numerical values of plots are provided in Figure 6-source data 1. The time courses were not significantly different ($p = 0.12$ from ANOVA). Numerical values of plots are provided in Figure 6-source data 1.

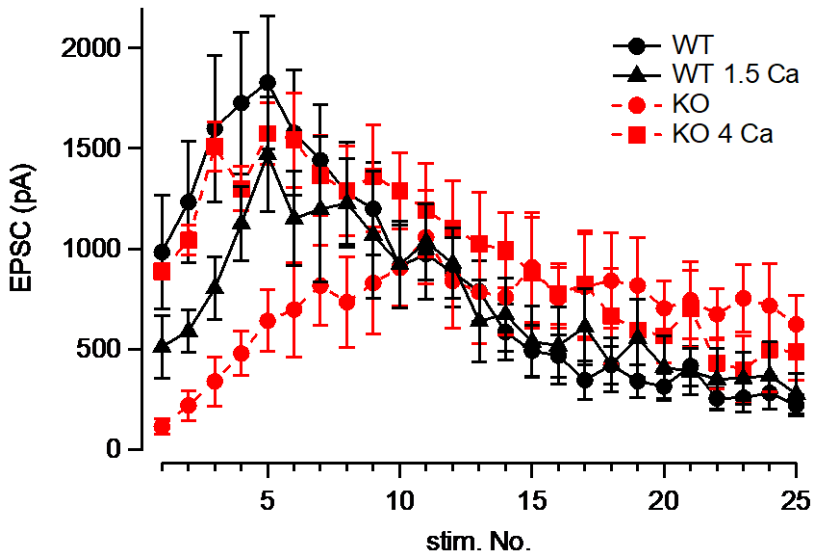

Figure 6-figure supplement 1. The EPSC amplitudes plotted against the stimulus number

The same data set as Fig. 6C-Fig. 6E, but the absolute EPSC amplitudes are plotted instead

of the normalized amplitudes. Numerical values of plots are provided in Figure 6-source data 1. Raw data were summarized. In Fig. 5 and Fig. 6, the effect of holding potential was corrected so that the values were adjusted to those at -70 mV. Numerical values of plots are provided in Figure 6-source data 1.

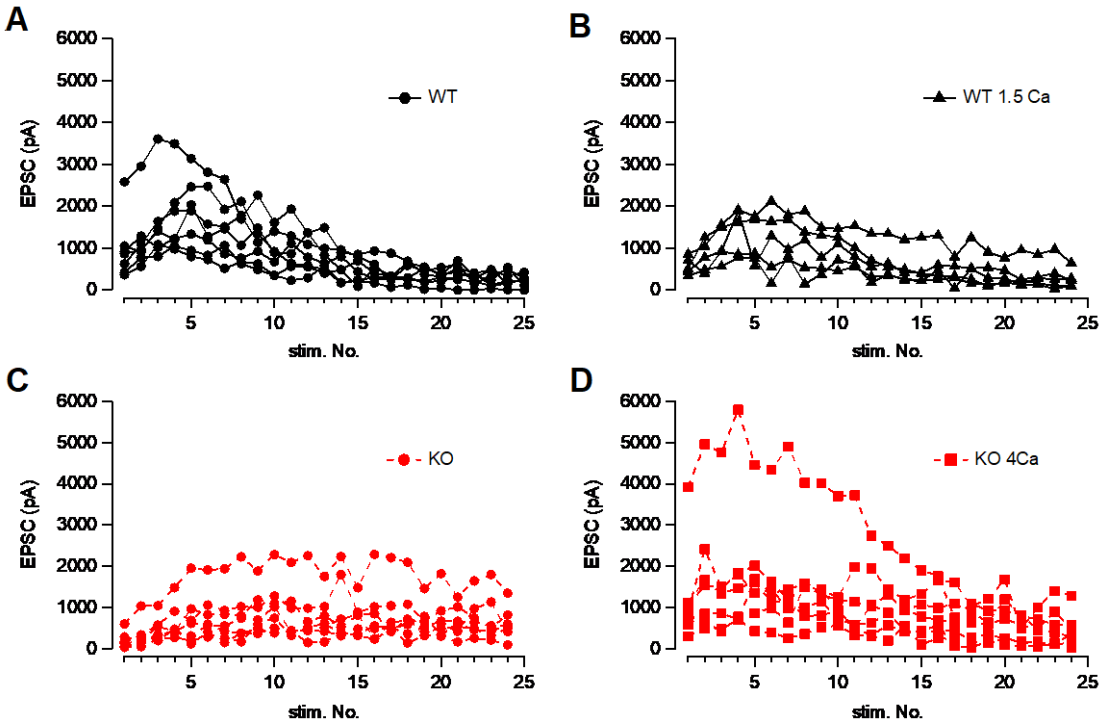

Figure 6-figure supplement 2. The individual data of Fig. 6

WT in 2mM (**A**) and 1.5 mM (**B**) $[Ca^{2+}]_{ext}$, and KO in 2 mM (**C**) and 4 mM $[Ca^{2+}]_{ext}$ (**D**) are shown. Numerical values of plots are provided in Figure 6-source data 1.

Figure 6-source data 1. Datasets of numerical values presented in Figure 6, Figure 6-figure supplement 1, and Figure 6-figure supplement 2.

405 **STED microscopy reveals that RIM-BP2 KO reduces the density of P/Q-type Ca^{2+}**
406 **channels.**

407 Our electrophysiological data suggest that RIM-BP2 may regulate the density of
408 Ca^{2+} channels. In order to directly study the Ca^{2+} channel density at the AZ, we performed
409 STED microscopy analysis of Ca^{2+} channels in WT and RIM-BP2 KO hippocampal mossy
410 fiber terminals. We here focused on P/Q-type and N-type Ca^{2+} channels because both Ca^{2+}
411 channel types are relevant for transmitter release at this synapse (Castillo et al., 1994; Pelkey
412 et al., 2006; Li et al., 2007). We performed immunohistochemistry on thin brain cryosections
413 from WT and RIM-BP2 KO mice. STED microscopy confirmed complete loss of RIM-BP2
414 proteins in KO terminals (Figure 7-figure supplement 1). We then immunohistochemically
415 labeled the α-subunit of either P/Q-type Ca^{2+} channel (Cav2.1) or N-type Ca^{2+} channel
416 (Cav2.2) and Munc13-1 (AZ/release site marker, Böhme et al., 2016; Sakamoto et al., 2018)
417 with VGLUT1 (presynaptic marker) and PSD-95 (postsynaptic marker) (Fig. 7A, Fig. 7B and
418 Figure 7-figure supplement 2). In the stratum lucidum of the hippocampal CA3 region, mossy
419 fibers form large synapses containing multiple and clustered AZs on CA3 pyramidal cells,
420 and also small en passant and filopodial synapses containing a single AZ on interneurons
421 (Acsády et al., 1998; Rollenhagen et al., 2007). Consistent with this, large VGLUT1 positive
422 terminals rarely contacted interneurons marked with two major interneuron markers,

423 mGluR1α and GluA4 (Figure 7-figure supplement 3). Thus, we identified AZs using Munc13-
424 1 STED images and quantified the signal intensity of Cav2.1 or Cav2.2 only at AZs clustered
425 in large VGLUT1 positive terminals in the CA3 stratum lucidum, allowing us to confine the
426 analysis to large mossy fiber terminals innervating onto CA3 pyramidal cells. The total signal
427 intensity of Cav2.1 at the AZ was 22% lower in RIM-BP2 KO mice (n = 4 animals) than in WT
428 mice (n = 4 animals) (p = 0.0286) (Fig. 7C, left). These data are consistent with the reduction
429 of Ca^{2+} currents in RIM-BP2 KO mice (Fig. 1), though STED microscopy is non-linear and
430 can only provide qualitative differences regarding intensity. In addition, the spatial resolution
431 of STED microscopy (especially z axis) does not assign the signals to the large mossy fiber
432 terminal rigidly.

433 In contrast to Cav2.1, the total signal intensity of Cav2.2 and Munc13-1 did not
434 significantly differ between WT and RIM-BP2 KOs (p = 0.3143 and p = 0.0831) (Fig. 7C,
435 right), though it remains possible that we failed to detect some changes. Furthermore, we
436 found that the number of Cav2.1 clusters within the AZ identified by STED deconvolution
437 analysis was not altered (2.5 ± 0.11 in WT, n = 4 animals; 2.3 ± 0.02 in KO, n = 4 animals) (p
438 = 0.114). These data suggest that RIM-BP2 KO reduces the number of P/Q-type Ca^{2+}
439 channels per cluster. To optically estimate physical distances between Ca^{2+} channels and
440 release sites, we next analyzed the nearest neighboring distance between Cav2.1 and

441 Munc13-1 clusters. These distances were unchanged (61 ± 1.4 nm in WT, n = 4 animals; 64

442 ± 1.3 nm in KO, n = 4 animals) (p = 0.200) (Fig. 7D), consistent with the similar sensitivity of

443 release to EGTA between WT and RIM-BP2 KO mice. However, the resolution of STED

444 microscopy cannot allow detection of small differences of the cluster number and the distance

445 between WT and KO. From these results together with presynaptic recordings, we conclude

446 that decreased Ca^{2+} influx in RIM-BP2 KO hippocampal mossy fiber terminals is caused by

447 reduction in the density of P/Q-type Ca^{2+} channels at the AZ.

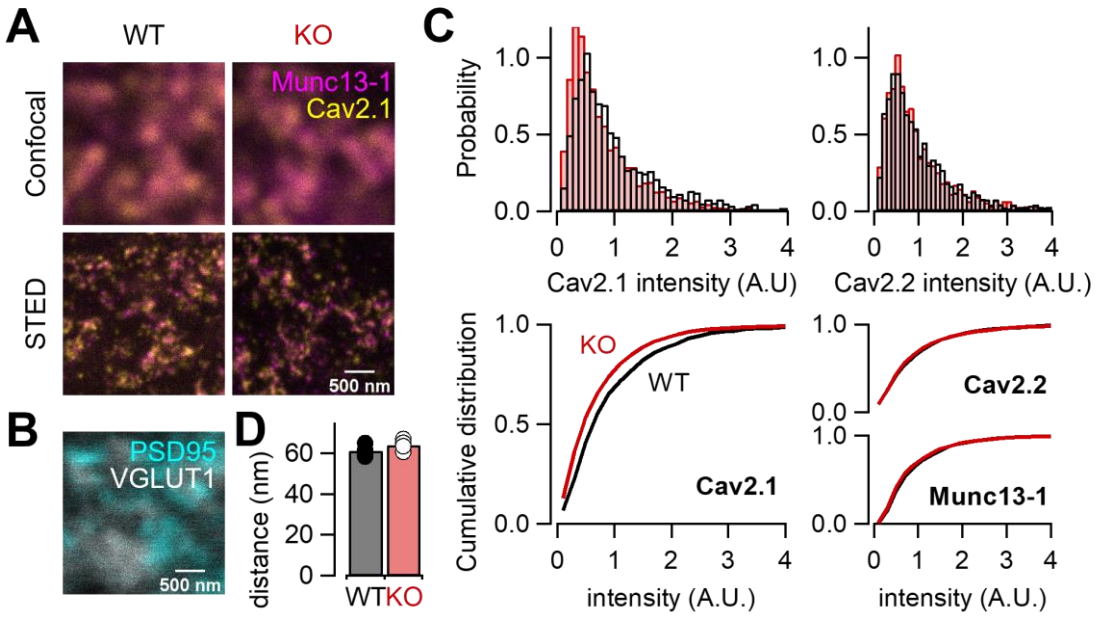

448

449 **Figure 7. RIM-BP2 deletion alters the density of Cav2.1 clusters within the AZ**

450 (**A**) Confocal *(top)* and STED *(bottom)* images of Munc13-1 (magenta) and Cav2.1 (yellow)

451 clusters at hippocampal mossy fiber terminals of WT *(left)* and RIM-BP2 KO *(right)* mice.

452 (Scale bar: 500 nm.) (**B**) Confocal images of PSD95 (cyan) and VGLUT1 (white) to identify

glutamatergic synapses in CA3 stratum lucidum: mossy fiber-CA3 synapses. (Scale bar: 500 nm.) The image is taken from same region shown in (**A**), *(left)*. (**C**) Histograms *(top)* and cumulative distribution plots *(bottom)* of the total signal intensity of Cav2.1 *(left)*, Cav2.2, and Munc13-1 *(right)* at AZs in WT (black) and RIM-BP2 KO (red) mice. (**D**) The average nearest neighbor distance between Cav2.1 and Munc13-1 clusters in WT (black; n = 4 animals) and RIM-BP2 KO (red; n = 4 animals) mice. Several hundreds of AZs per image were analyzed. Data show the average value of distance per animal and error bars represent SEM. Each data point indicates individual values. Numerical values of plots are provided in Figure 7-source data 1.

Figure 7-source data 1. Datasets of numerical values presented in Figure 7.

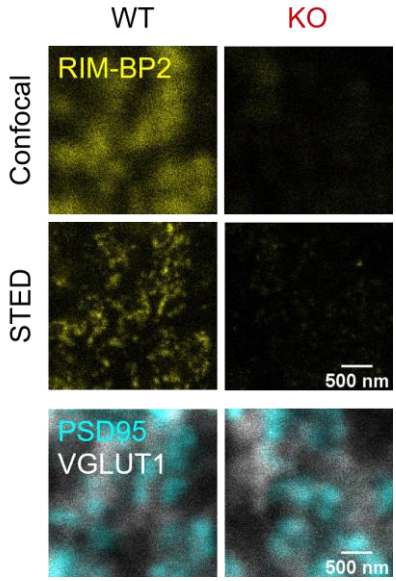

Figure 7-figure supplement 1. STED microscopy confirmed loss of RIM-BP2 proteins

466 **in KO terminals**

467 Confocal *(top)* and STED *(middle)* images of RIM-BP2 (yellow) in WT *(left)* and RIM-BP2 KO

468 *(right)* hippocampal mossy fiber terminals identified by PSD95 (cyan) and VGLUT1 (white)

469 *(bottom)*. (Scale bar: 500 nm.) The *bottom* images show the same region as *top* and *middle*.

470

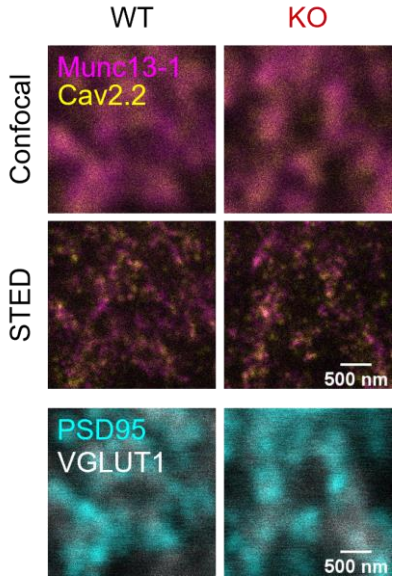

471

472 **Figure 7-figure supplement 2. STED imaging of Cav2.2 at hippocampal mossy fiber**

473 **terminals**

474 Confocal *(top)* and STED *(middle)* images of Munc13-1 (magenta) and Cav2.2 (yellow)

475 clusters in WT *(left)* and RIM-BP2 KO *(right)* mice. Confocal images of PSD95 (cyan) and

476 VGLUT1 (white) in the same region as *top* and *middle* are also shown *(bottom)*. (Scale bar:

477 500 nm.)

478

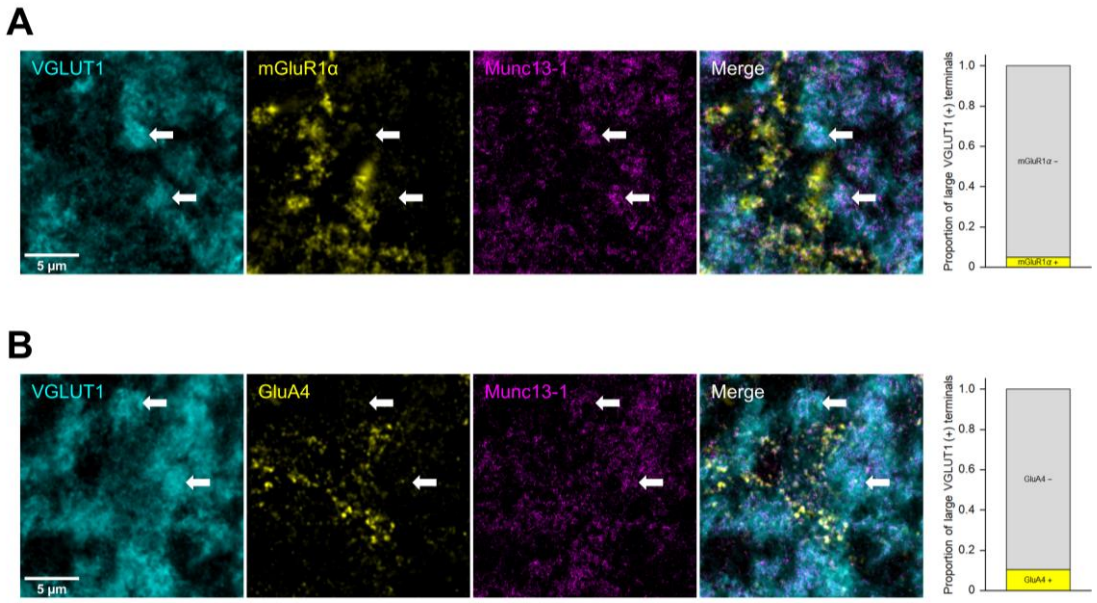

Figure 7-figure supplement 3. Immunohistochemical characterization of large VGLUT1 positive terminals in the CA3 stratum lucidum

(**A**) Confocal images of VGLUT1 (cyan) and mGluR1α (yellow) were taken with STED images of Munc13-1 (magenta) in the CA3 stratum lucidum. Arrows indicate representative large MF terminals identified by VGLUT1 signals (Scale bar: 5 μm.) The right graph shows the proportion of large VGLUT1 positive terminals contacting mGluR1α positive processes. (**B**) Same as (**A**) but for GluA4 instead of mGluR1α. (Scale bar: 5 μm.)

Discussion

Accumulation of Ca^{2+} channels at the AZ, and efficient vesicle docking and priming are essential factors for fast synaptic vesicle exocytosis. AZ proteins are critical for fast

491 synchronous release and synaptic diversity. RIM-BPs have been implicated in recruitment of
492 Ca^{2+} channels to the AZ (Kaeser et al., 2011; Liu et al., 2011) by interacting with RIMs and
493 Ca^{2+} channels (Wang et al., 2000; Hibino et al., 2002). In addition, RIM-BPs, like RIM1/2,
494 recruit Munc-13 and accelerate synaptic vesicle priming (Brockmann et al., 2020). At murine
495 central synapses, RIM-BPs deficient synapses demonstrate overall a rather mild decrease
496 in the amounts of transmitter release (Acuna et al., 2015; Grauel et al., 2016; Luo et al., 2017;
497 Krinner et al., 2017; Brockmann et al., 2019; Butola et al., 2021). Most studies so far have
498 been mainly focused on synapses with high release probability (phasic synapses) such as
499 the calyx of Held and CA3-CA1 synapses. That said, at mossy fiber-CA3 synapses, KO of
500 RIM-BPs has a strong influence on synaptic transmission (Brockmann et al., 2019). Notably,
501 at mossy fiber-CA3 synapses, release probability is relatively low (tonic synapses). It was
502 unknown whether the reduction of transmitter release at RIM-BP2 KO mossy fiber synapses
503 is due to impaired Ca^{2+} channel recruitment, and / or impaired vesicle docking or priming.
504 Using STED microscopy, Brockmann et al. (2019) suggested that the physical recruitment of
505 Munc13-1 might be an important function of RIM-BP2, though functional demonstration had
506 been lacking.

507 By using direct presynaptic patch clamp recordings, we here observed a decrease
508 of Ca^{2+} current amplitudes (~30%) in RIM-BP2 KO mice (Fig. 1). Consistently, STED

microscopy supported decreased density of P/Q-type Ca^{2+} channels (Cav2.1) in the mutant mossy fiber terminal (Fig. 7). Brockmann et al. (2019) observed a reduction of Munc13-1 cluster number and docked vesicles in RIM-BP2 deficient synapses at hippocampal mossy fiber terminals (Fig. 7). They identified the terminals by using ZnT3, enriched at mossy fiber (Brockmann et al., 2019; Wenzel et al., 1997). Our STED imaging did not detect differences in Munc13-1 cluster number at the AZ between WT and RIM-BP2 KO mice. Notably, we analyzed the number of Cav2.1, Cav2.2 and Munc13-1 clusters only within AZs showing direct co-localization with VGLUT1 and PSD-95, which mainly reflects the AZs facing CA3 pyramidal cells rather than the synapses onto interneurons (Acsády et al., 1998; Rollenhagen et al., 2007). Such a difference in areas analyzed between previous and our study might explain the difference. In addition, some developmental variability/compensation could still occur in the range we studied and be relevant for the discrepancy between Munc13-1 results between Brockmann et al. (2019) and this study. Also, the spatial resolution of our study is limited and we cannot rigidly measure the signals only from large mossy fiber terminals. It is important to state that our results do not exclude roles of RIM-BP2 in synaptic vesicle priming. Indeed, we have shown that the reduction of the EPSC amplitudes could not be fully explained by the reduced Ca^{2+} influx (Fig. 5). Because the differences in the RRP size measured from capacitance measurements were relatively minor (Fig. 1-Fig. 3), it is likely

527 that the fusion competence was impaired by RIM-BP2 KO, but this could be overcome by
528 large Ca^{2+} influx. Consistently, the EPSCs responses of KO became larger and comparable
529 to those of WT (Fig. 6A, Fig. 6B, and Figure 6-figure supplement 1) during repetitive AP
530 stimulation, at least qualitatively.

531 Recent studies have reported that RIM-BPs deletion altered Ca^{2+} channel
532 localization and loosened the coupling between Ca^{2+} channels and synaptic vesicles at
533 phasic synapses (Acuna et al., 2015; Grauel et al., 2016; Butola et al., 2021). We investigated
534 the Ca^{2+} channel-vesicle coupling at hippocampal mossy fiber terminals. The sensitivity of
535 release to Ca^{2+} chelator EGTA was not changed between WT and RIM-BP2 KO mice. We
536 also indicated RIM-BP2 KO does not alter the coupling of Ca^{2+} channels to release sites by
537 using STED microscopy, though spatial resolution of STED microscopy in this study could
538 not allow to detect small changes (Fig. 7) .

539 At phasic synapses, deletion of RIM-BP2 affects physical distance between Ca^{2+}
540 channels and synaptic vesicles. In contrast, at hippocampal mossy fiber terminals having low
541 release probability (Vyleta and Jonas, 2014), RIM-BP2 KO decreased the number of P/Q-
542 type Ca^{2+} channels, thereby reducing Ca^{2+} influx and neurotransmitter release. Thus, we
543 hypothesize the specific molecular-architectural and biochemical contributions by RIM-BPs
544 might be of different relevance between phasic and tonic synapses. Brockmann et al. (2020)

545 proposed that RIM-BP2 controls Ca^{2+} channel recruitment and vesicle priming by profound
546 interaction with RIMs and Munc13s. These results have been obtained through studying
547 hippocampal cultures dominated by phasic synapses. It seems possible that the interaction
548 among three protein types is tight at phasic synapses, simply because of high density of
549 these proteins at AZs. Alternatively, one might speculate about additional proteins, different
550 interaction surfaces taken, transsynaptic columns (Tang et al., 2016). Deletion of RIM-BP2
551 does not lead to loss of Ca^{2+} channels themselves and/or vesicle priming due to remaining
552 RIMs, Munc13, and other proteins, which can regulate recruitment of Ca^{2+} channels and
553 synaptic vesicle priming without RIM-BP2. Instead, fine-tuning of release such as
554 synchronization is compromised. We hypothesize that AZ scaffold might be differently built,
555 leading to different consequences when eliminating one component. Hence deletion of RIM-
556 BP2 leads to immediate loss of Ca^{2+} channels and vesicle priming. This is in line with the
557 proposal that at tonic synapses, synaptic vesicles are only loosely coupled with Ca^{2+}
558 channels (Vyleta and Jonas, 2014) and vesicles are de-primed under resting conditions (Miki
559 et al., 2016; Neher and Brose, 2018). Future research along this line may lead to an
560 understanding of how fine molecular differences in the AZ scaffolds might orchestrate
561 synaptic diversity.

562 Although this study reveals reduction of Ca^{2+} currents and reduced fusion

563 competence in RIM-BP2 KO mossy fiber synapses, it has some limitation. Most importantly,
564 with conventional knockouts the observed changes could reflect compensatory
565 developmental changes and not direct outcomes of the RIM-BP2 knockout. This issue should
566 be resolved by using region-specific and time-dependent conditional KO.
567

568 **Materials and Methods**

569 **Slice preparation**

570 All animal experiments were conducted in accordance with the guidelines of the
571 Physiological Society of Japan, and were approved by Doshisha University Animal
572 Experiment Committee (A22063, D22063).

573 We used male and female C57BL/6 mice (postnatal days 35-40). WT and RIM-BP2
574 KO mice (Grauel et al., 2016) were deeply anesthetized with isoflurane and decapitated.
575 Their brains were quickly removed and chilled in sherbet-like cutting solution containing (in
576 mM): 87 NaCl, 75 sucrose, 25 $NaHCO_3$, 1.25 NaH_2PO_4, 2.5 KCl, 10 glucose, 0.5 $CaCl_2$ and
577 7 $MgCl_2$ bubbled with 95% O_2 and 5% CO_2 (Hallermann et al., 2003). Hippocampal slices
578 (300 μm thick) were prepared from brains using a vibratome (VT1200S, Leica) in ice-cold
579 cutting solution. After slicing, slices were incubated in cutting solution at 37°C for 30 min, and
580 subsequently kept at room temperature (22-25°C) up to 4 h.

581

582 **Whole-cell recordings**

583 Electrophysiological recordings were performed in a recording chamber filled with

584 the extracellular solution containing (in mM): 125 NaCl, 2.5 KCl, 25 glucose, 25 $NaHCO_3$,

585 1.25 NaH_2PO_4, 0.4 ascorbic acid, 3 myo-inositol, 2 Na-pyruvate, 2 $CaCl_2$ and 1 $MgCl_2$

586 saturated with 95% O_2 and 5% CO_2. In some experiments, the concentration of $CaCl_2$ was

587 changed to 1 mM, 1.5 mM and 4 mM. For presynaptic membrane capacitance

588 measurements, 1 μM tetrodotoxin (TTX, Wako) was added to block Na^+ channels.

589 Moreover, for recording Ca^{2+} currents (Fig. 1B), 10 mM TEA-Cl was added to block K^+

590 channels. Slices were visualized by an upright microscope (BX-51, Olympus). Whole-cell

591 patch-clamp recordings were applied to hippocampal mossy fiber terminals and CA3

592 pyramidal cells at room temperature. The patch pipettes were filled with the intracellular

593 solution containing (in mM): 135 Cs-gluconate, 20 TEA-Cl, 10 Hepes, 5 Na_2-

594 phosphocreatine, 4 MgATP, 0.3 GTP and 0.5 EGTA (pH = 7.2 adjusted with CsOH). In

595 some experiments, the concentration of EGTA was changed to 5 mM. Presynaptic patch

596 pipettes (BF150-86-10, Sutter Instrument) had a resistance of 15-20 MΩ and series

597 resistance (R_s) was 30-70 MΩ. R_s was compensated so that residual resistance was 30-35

598 MΩ. For postsynaptic recordings, the same internal solution was used, except that EGTA

599 concentration was raised to 5 mM. Postsynaptic patch pipettes (BF150-86-10, Sutter

600 Instrument) had a resistance of 3-7 MΩ and series resistance (R_s) was 5-20 MΩ which was

601 compensated by 50-80 %.

602 Patch-clamp recordings were performed using an EPC10/3 or EPC10/2 amplifier

603 (HEKA) in voltage-clamp mode, controlled by Patchmaster software (HEKA). Membrane

604 currents were low-pass filtered at 2.9 kHz and sampled at 20 or 50 kHz.

605 Membrane capacitance measurements were performed using an EPC10/3

606 amplifier in the sine + DC configuration (Gillis, 2000) using Patchmaster software (HEKA). A

607 sine wave (30 mV in amplitude, 1000 Hz in frequency) was superimposed on the holding

608 potential of -80 mV. The terminal was depolarized from -80 mV to +10 mV for 5-100 ms.

609 The IV of presynaptic Ca currents were measured by sequential depolarized for 5 ms, with

610 2 ms intervals from -80 mV to +70 mV by 10 mV steps.

611 For the EPSC measurements, postsynaptic cells (CA3 pyramidal cells) were

612 voltage clamped at -60 ~ -80 mV. For Figs. 5 and 6, the data were corrected for the

613 different holding potential (re-calculated to the value at -70 mV assuming the reversal

614 potential of 0 mV, which may have the correction of ~15 %). At the end of the experiments,

615 DCG-Ⅳ was applied to confirm mossy fiber synaptic responses, whenever possible. The

616 mossy fibers were stimulated extracellularly using a glass electrode used for patch clamp
617 containing the extracellular solution and the stimulation intensity was usually 10-60 V.
618 Data were obtained from at least three different WT and RIM-BP2 KO terminals in
619 each set of experiments (biological replicate).
620
621 **Immunostaining**
622 Brains of WT and RIM-BP2 KO mice were quickly removed and transferred to
623 cryomold (Sakura Finetek) filled with tissue freezing medium (Leica). Brains were
624 instantaneously frozen on aluminum block in liquid nitrogen and stored at -80°C. For
625 cryosectioning, frozen brains were kept in cryostat (CM1860, Leica) at -18°C for 30 min.
626 Then, 10 μm-thick sections were sliced and collected on cover glasses (Matsunami glass,
627 25×25 No.1). Sections were quickly fixed by dehydration with a heat blower at 50°C for 1
628 min, and further dehydrated in ethanol for 30 min at -25°C and in acetone for 10 min on ice.
629 After blocking with PBS containing 0.3% BSA at room temperature, sections were
630 incubated with primary antibodies diluted in PBS containing 0.3% BSA: anti-VGLUT1
631 (1:2000, Synaptic Systems, guinea pig polyclonal, RRID:AB_887878), anti-PSD-95 (1:50,
632 NeuroMab, mouse monoclonal IgG2a, clone K28/43, TC Supernatant, RRID:AB_2877189),
633 anti-Munc13-1 (1:1000, mouse monoclonal IgG1, clone 11B-10G, Sakamoto et al., 2018),

634 and anti-Cav2.1 (1:400, Synaptic Systems, rabbit polyclonal, RRID:AB_2619841) or anti-
635 Cav2.2 (1:400, Synaptic Systems, mouse monoclonal IgG2b, clone 163E3,
636 RRID:AB_2619843) or anti-RIM-BP2 (1:200, mouse monoclonal IgG2b, clone 8-4G,
637 Sakamoto et al., 2022) for 3 hours at room temperature. Afterwards, sections were washed
638 and incubated with fluorescence dye labeled secondary antibodies: DyLight 405 Anti-
639 Guinea Pig IgG (Jackson ImmunoResearch, RRID:AB_2340470), Alexa Fluor 488 (Thermo
640 Fisher Scientific) labeled Anti-Mouse IgG2a (Jackson ImmunoResearch,
641 RRID:AB_2338462), STAR635P (Abberior) labeled Anti-Mouse IgG1 (Jackson
642 ImmunoResearch, RRID:AB_2338461), and Alexa Fluor 594 (Thermo Fisher Scientific)
643 labeled Anti-Rabbit IgG (Jackson ImmunoResearch, RRID:AB_2340585) or Anti-Mouse
644 IgG2b (Jackson ImmunoResearch, RRID:AB_2338463) for 1 hour at room temperature.
645 Sections were post-fixed with 4% PFA in PBS and washed with PBS. Sections were
646 mounted on coverslips using Prolong Glass Antifade Mountant (Thermo Fisher Scientific).
647 The same number of sections were obtained from WT and RIM-BP2 KO brains and
648 processed in parallel at the same experimental day (biological replicate).
649 For Figure 7-figure supplement 3, only WT brains were used. Primary antibodies
650 used were anti-VGLUT1 (1:2000, Synaptic Systems, rabbit polyclonal, RRID:AB_887877),
651 anti-VGLUT1 (1:2000, Synaptic Systems, guinea pig polyclonal, RRID:AB_887878), anti-

652 mGluR1α (1:200, Nittobo Medical, guinea pig polyclonal, mGluR1a-GP-Af660), anti-
653 GluA4C (1:100, Nittobo Medical, rabbit polyclonal, GluR4C-Rb-Af160), and anti-Munc13-1
654 (1:1000, mouse monoclonal IgG1, clone 11B-10G).
655
656 **STED imaging**
657 STED imaging was performed using TCS SP8 STED 3x microscope (Leica)
658 equipped with a 405 nm diode laser, a pulsed white light laser (WLL), a continuous 592 nm
659 STED laser for alignment, a pulsed 775 nm STED laser, HyD detectors, and a 100× oil-
660 immersion objective lens (NA = 1.4). STED images were acquired using the Leica LAS-X
661 software with an image format of 1024×1024 pixels, 16-bit sampling, 8-line accumulations,
662 and 11.36-zoom factor, yielding a pixel size of 10 nm. HyD detectors were configured to
663 counting mode with a gating from 0.5 to 6.5 nanosecond. A 405 nm diode laser was used to
664 excite DyLight405. Alexa488, Alexa594, and STAR635P were excited using WLL at 488
665 nm, 561 nm, and 633 nm, respectively. The 775 nm STED laser power was set to 75% and
666 100% of maximum power for depletion of STAR635P and Alexa594, respectively, and delay
667 time was set to 300 picoseconds. STED imaging was performed on thin sections obtained
668 from four different WT and RIM-BP2 KO mice (biological replicate). Images were acquired
669 three times from each section (technical replicate).

Analysis

For electrophysiological experiments, the data were analyzed by Igor Pro (WaveMetrics) or Excel (Microsoft Corp). Presynaptic calcium currents were measured at the peak amplitude during the depolarizing pulse. Capacitance jumps were measured between baseline (before the pulse) and ~10 ms after the pulse where the effect of tail currents became minor. To determine the time constant of release, an exponential fit was applied. Values are given as mean ± SEM, and n indicates the number of recorded terminals or the number of animals used. Statistical method of sample size determination was not done, but our sample sizes are similar to those of previous studies (Hallermann et al., 2003, Midorikawa and Sakaba, 2017).

For STED imaging, data were analyzed using custom-designed programs in Mathematica (Wolfram), values were processed by Igor Pro (WaveMetrics), and pictures were created with ImageJ (NIH). To determine the area of AZs, image masks were generated from STED images of Munc13-1 by unsharp masking and image binarization. Only AZs that show co-localization with VGLUT1 and PSD-95 immunofluorescence signals were included in the analysis. To confine the analysis to the large mossy fiber boutons, AZs in presynaptic terminals of small VGLUT1-positive area were excluded. Then, the

background subtracted integral of signal intensity of Cav2.1 or Cav2.2 was quantified using the image masks of AZs. The background signal intensity was estimated from non-AZ area in the same STED images. For quantification of Cav2.1 clusters in the AZs, STED images of Cav2.1 were deconvolved using a gaussian kernel with a radius of 40 nm. Image masks of each Ca^{2+} channel were generated from deconvolved STED images by unsharp masking and image binarization. Then, the total signal intensity, the size, and the number of Cav2.1 clusters at the AZs were quantified using the image masks of Cav2.1 clusters. Custom-designed programs in Mathematica (Wolfram) are available from Source code 1. Values are given as mean ± SEM, and n indicates the number of animals. Statistical method of sample size determination was not done, but our sample sizes are similar to those of previous studies (Brockmann et al., 2019).

Experiments were not fully randomized and blinded.

Statistical analysis was done in MATLAB (The MathWorks) or SPSS (IBM). t-test, ANOVA, and mixed model were used for statistical tests. Significance level was set at $\alpha = 0.05$, and p values were described in the main text or figure legends.

Data availability

All data generated in this study are included in the main text or shown as scatter

plots in each graph. Numerical values of graphs are provided in Source data files. The custom-written code files in Mathematica are uploaded as Source code file.

Acknowledgements

We thank Stephan Sigrist, Dietmar Schmitz and Christian Rosenmund for kindly providing us RIM-BP2 KO mice. We also thank Stephan Sigrist for comments on the manuscript and The IRCN Imaging Core, The University of Tokyo Institutes for Advanced Studies, for the use of STED microscopy and for assistance. This works has been supported by JSPS KAKENHI (JP20J20550 to RM, JP20KK0171, JP21K15183 to HS, JP20H03427 to KH, JP20KK0171, JP21H02598 to TS), JSPS Core-to-Core program A. Advanced Research Networks (JPJSCCA2022007 to TS) and JST, PRESTO (JPMJPR21E7 to HS).

Competing interests

None

Additional information

Author ORCIDs

Rinako Miyano https://orcid.org/0000-0002-0022-7198

Hirokazu Sakamoto https://orcid.org/0000-0002-9881-5173

Kenzo Hirose https://orcid.org/0000-0002-8944-6513

Takeshi Sakaba https://orcid.org/0000-0003-0688-7717

References

Acsády L, Kamondi A, Sík A, Freund T, Buzsáki G. 1998. GABAergic cells are the major postsynaptic targets of mossy fibers in the rat hippocampus. *Journal of Neuroscience* **18**:3386-3403. DOI: https://doi.org/10.1523/JNEUROSCI.18-09-03386.1998, PMID: 9547246

Acuna C, Liu X, Gonzalez A, Südhof TC. 2015. RIM-BPs Mediate Tight Coupling of Action Potentials to Ca^{2+}-Triggered Neurotransmitter Release. *Neuron* **87**:1234-1247. DOI: https://doi.org/10.1016/j.neuron.2015.08.027, PMID: 26402606

Adler EM, Augustine GJ, Duffy SN, Charlton MP. 1991. Alien intracellular calcium chelators attenuate neurotransmitter release at the squid giant synapse. *Journal of Neuroscience* **11**:1496-1507. DOI: https://doi.org/10.1523/JNEUROSCI.11-06-01496.1991, PMID: 1675264

Blatow M, Caputi A, Burnashev N, Monyer H, Rozov A. 2003. Ca^{2+} buffer saturation underlies paired pulse facilitation in calbindin-D28k-containing terminals. *Neuron* **38**: 79-88. DOI: https://doi.org/10.1016/s0896-6273(03)00196-x, PMID: 12691666

Bollmann JH, Sakmann B, Borst JG. 2000. Calcium sensitivity of glutamate release in a calyx-type terminal. *Science* **289**: 953-957. DOI: https://doi.org/10.1126/science.289.5481.953, PMID: 10937999

Borst JG, Sakmann B. 1996. Calcium influx and transmitter release in a fast CNS synapse. *Nature* **383**:431-434. DOI: https://doi.org/10.1038/383431a0, PMID: 8837774

Brockmann MM, Maglione M, Willmes CG, Stumpf A, Bouazza BA, Velasquez LM, Grauel MK, Beed P, Lehmann M, Gimber N, Schmoranzer J, Sigrist SJ, Rosenmund C, Schmitz D. 2019. RIM-BP2 primes synaptic vesicles *via* recruitment of Munc13-1 at hippocampal mossy fiber synapses. *eLife* **8**:e43243. DOI: https://doi.org/10.7554/eLife.43243, PMID: 31535974

Brockmann MM, Zarebidaki F, Camacho M, Grauel MK, Trimbuch T, Südhof TC, Rosenmund C. 2020. A Trio of Active Zone Proteins Comprised of RIM-BPs, RIMs, and Munc13s Governs Neurotransmitter Release. *Cell Reports* **32**:107960-107960. DOI: https://doi.org/10.1016/j.celrep.2020.107960, PMID: 32755572

Butola T, Alvanos T, Hintze A, Koppensteiner P, Kleindienst D, Shigemoto R, Wichmann C, Moser T. 2021. RIM-Binding Protein 2 Organizes Ca^{2+} Channel Topography and Regulates Release Probability and Vesicle Replenishment at a Fast Central Synapse. *Journal of Neuroscience* **41**:7742-7767. DOI: https://doi.org/10.1523/JNEUROSCI.0586-21.2021, PMID: 34353898

Castillo PE, Weisskopf MG, Nicoll RA. 1994. The role of Ca^{2+} channels in hippocampal mossy fiber synaptic transmission and long-term potentiation. *Neuron* **12**:261-269. DOI: https://doi.org/10.1016/0896-6273(94)90269-0, PMID: 8110457

Dodge FA, Rahamimoff R. 1967. Co-operative action a calcium ions in transmitter release at the neuromuscular junction. *The Journal of physiology* **193**:419-432. DOI: https://doi.org/10.1113/jphysiol.1967.sp008367, PMID: 6065887

Geiger JR, Jonas P. 2000. Dynamic control of presynaptic Ca^{2+} inflow by fast-inactivating K^+ channels in hippocampal mossy fiber boutons. *Neuron* **28**: 927-939. DOI: https://doi.org/10.1016/s0896-6273(00)00164-1, PMID: 11163277

Grauel MK, Maglione M, Reddy-Alla S, Willmes CG, Brockmann MM, Trimbuch T, Rosenmund T, Pangalos M, Vardar G, Stumpf A, Walter AM, Rost BR, Eickholt BJ, Haucke V, Schmitz D, Sigrist SJ, Rosenmund C. 2016. RIM-binding protein 2 regulates release probability by fine-tuning calcium channel localization at murine hippocampal synapses. *PNAS* **113**:11615-11620. DOI: https://doi.org/10.1073/pnas.1605256113, PMID: 27671655

Hallermann S, Pawlu C, Jonas P, Heckmann M. 2003. A large pool of releasable vesicles in a cortical glutamatergic synapse. *PNAS* **100**:8975-8980. DOI: https://doi.org/10.1073/pnas.1432836100, PMID: 12815098

Hibino H, Pironkova R, Onwumere O, Vologodskaia M, Hudspeth AJ, Lesage F. 2002. RIM binding proteins (RBPs) couple Rab3-interacting molecules (RIMs) to voltage-gated Ca^{2+} channels. *Neuron* **34**:411-423. DOI: https://doi.org/10.1016/s0896-6273(02)00667-0, PMID: 11988172

Kaeser PS, Deng L, Wang Y, Dulubova I, Liu X, Rizo J, Südhof TC. 2011. RIM proteins tether Ca^{2+} channels to presynaptic active zones via a direct PDZ-domain interaction. *Cell* **144**:282-295. DOI: https://doi.org/10.1016/j.cell.2010.12.029, PMID: 21241895

Katz B. 1969. The release of neural transmitter substances. Liverpool University Press. ISBN: 0853230609

Krinner S, Butola T, Jung S, Wichmann C, Moser T. 2017. RIM-Binding Protein 2 Promotes a Large Number of $Ca_V1.3$ Ca^{2+}-Channels and Contributes to Fast Synaptic Vesicle Replenishment at Hair Cell Active Zones. *Frontiers in Cellular Neuroscience* **11**:334. DOI: https://doi.org/10.3389/fncel.2017.00334, PMID: 29163046

Li L, Bischofberger J, Jonas P. 2007. Differential gating and recruitment of P/Q-, N-, and R-type Ca^{2+} channels in hippocampal mossy fiber boutons. *Journal of Neuroscience* **27**:13420-13429. DOI: https://doi.org/10.1523/JNEUROSCI.1709-07.2007, PMID: 18057200

Lindau M, Neher E. 1988. Patch-clamp techniques for time-resolved capacitance measurements in single cells. *Pflügers Archiv* **411**:137-146. DOI: https://doi.org/10.1007/BF00582306, PMID: 3357753

Liu KS, Siebert M, Mertel S, Knoche E, Wegener S, Wichmann C, Matkovic T, Muhammad K, Depner H, Mettke C, Bückers J, Hell SW, Müller M, Davis GW, Schmitz D, Sigrist SJ. 2011. RIM-binding protein, a central part of the active zone, is essential for neurotransmitter release. *Science* **334**:1565-1569. DOI: https://doi.org/10.1126/science.1212991, PMID: 22174254

Luo F, Liu X, Südhof TC, Acuna C. 2017. Efficient stimulus-secretion coupling at ribbon synapses requires RIM-binding protein tethering of L-type Ca^{2+} channels. *Proceedings of the National Academy of Sciences* **114**:E8081-E8090. DOI: https://doi.org/10.1073/pnas.1702991114, PMID: 28874522

Midorikawa M, Sakaba T. 2017. Kinetics of Releasable Synaptic Vesicles and Their Plastic Changes at Hippocampal Mossy Fiber Synapses. *Neuron* **96**:1033-1040.e3. DOI: https://doi.org/10.1016/j.neuron.2017.10.016, PMID: 29103807

Miki T, Malagon G, Pulido C, Llano I, Neher E, Marty A. 2016. Actin- and Myosin-Dependent Vesicle Loading of Presynaptic Docking Sites Prior to Exocytosis. *Neuron* **91**:808-823. DOI: https://doi.org/10.1016/j.neuron.2016.07.033, PMID: 27537485

Mittelstaedt T, Schoch S. 2007. Structure and evolution of RIM-BP genes: identification of a novel family member. *Gene* **403**:70-79. DOI: https://doi.org/10.1016/j.gene.2007.08.004, PMID: 17855024

Müller M, Genç Ö, Davis GW. 2015. RIM-binding protein links synaptic homeostasis to the stabilization and replenishment of high release probability vesicles. *Neuron* **85**:1056-1069. DOI: https://doi.org/10.1016/j.neuron.2015.01.024, PMID: 25704950

Neher E, Brose N. 2018. Dynamically Primed Synaptic Vesicle States: Key to Understand Synaptic Short-Term Plasticity. *Neuron* **100**:1283-1291. DOI: https://doi.org/10.1016/j.neuron.2018.11.024, PMID: 30571941

Pelkey KA, Topolnik L, Lacaille J-C, McBain CJ. 2006. Compartmentalized Ca^{2+} channel regulation at divergent mossy-fiber release sites underlies target cell-dependent plasticity. *Neuron* **52**:497-510. DOI: https://doi.org/10.1016/j.neuron.2006.08.032, PMID: 17088215

Petzoldt AG, Götz TWB, Driller JH, Lützkendorf J, Reddy-Alla S, Matkovic-Rachid T, Liu S, Knoche E, Mertel S, Ugorets V, Lehmann M, Ramesh N, Beuschel CB, Kuropka B, Freund C, Stelzl U, Loll B, Liu F, Wahl MC, Sigrist SJ. 2020. RIM-binding protein couples synaptic vesicle recruitment to release sites. *Journal of Cell Biology* **219**:e201902059. DOI: https://doi.org/10.1083/jcb.201902059, PMID: 32369542

Rollenhagen A, Sätzler K, Rodríguez EP, Jonas P, Frotscher M, Lübke JHR. 2007. Structural determinants of transmission at large hippocampal mossy fiber synapses. *Journal of Neuroscience* **27**:10434-10444. DOI: https://doi.org/10.1523/JNEUROSCI.1946-07.2007, PMID: 17898215

Sakamoto H, Ariyoshi T, Kimpara N, Sugao K, Taiko I, Takikawa K, Asanuma D, Namiki S, Hirose K. 2018. Synaptic weight set by Munc13-1 supramolecular assemblies. *Nature neuroscience* **21**:41–49. DOI: https://doi.org/10.1038/s41593-017-0041-9, PMID: 29230050

Sakamoto H, Kimpara N, Namiki S, Hamada S, Ohtsuka T, Hirose K. 2022. Synapse type-specific molecular nanoconfigurations of the presynaptic active zone in the hippocampus identified by systematic nanoscopy [unpublished manuscript]. *bioRxiv* 2022.03.11.483942. DOI: https://doi.org/10.1101/2022.03.11.483942

Schneggenburger R, Meyer AC, Neher E. 1999. Released fraction and total size of a pool of immediately available transmitter quanta at a calyx synapse. *Neuron* **23**:399-409. DOI: https://doi.org/10.1016/s0896-6273(00)80789-8, PMID: 10399944

Schneggenburger R, Neher E. 2000. Intracellular calcium dependence of transmitter release rates at a fast central synapse. *Nature* **406**: 889-893. DOI: https://doi.org/10.1038/35022702, PMID: 10972290

Südhof TC. 2012. The presynaptic active zone. *Neuron* **75**:11-25. DOI: https://doi.org/10.1016/j.neuron.2012.06.012, PMID: 22794257

Tang AH, Chen H, Li TP, Metzbower SR, MacGillavry HD, Blanpied TA. 2016. A trans-synaptic nanocolumn aligns neurotransmitter release to receptors. *Nature* **536**:210-214. DOI: https://doi.org/10.1038/nature19058, PMID: 27462810

Thanawala MS, Regehr WG. 2013. Presynaptic calcium influx controls neurotransmitter release in part by regulating the effective size of the readily releasable pool. *Journal of Neuroscience* **33**:4625-4633. DOI: https://doi.org/10.1523/JNEUROSCI.4031-12.2013, PMID: 23486937

von Gersdorff H, Matthews G. 1996. Calcium-dependent inactivation of calcium current in synaptic terminals of retinal bipolar neurons. *Journal of Neuroscience* **16**:115-122. DOI: https://doi.org/10.1523/JNEUROSCI.16-01-00115.1996, PMID: 8613777

Vyleta NP, Jonas P. 2014. Loose coupling between Ca^{2+} channels and release sensors at a plastic hippocampal synapse. *Science* **343**:665-670. DOI: https://doi.org/10.1126/science.1244811, PMID: 24503854

Wadel K, Neher E, Sakaba T. 2007. The coupling between synaptic vesicles and Ca^{2+} channels determines fast neurotransmitter release. *Neuron* **53**:563-575. DOI: https://doi.org/10.1016/j.neuron.2007.01.021, PMID: 17296557

Wang Y, Sugita S, Südhof TC. 2000. The RIM/NIM family of neuronal C2 domain proteins. Interactions with Rab3 and a new class of Src homology 3 domain proteins. *Journal of Biological Chemistry* **275**:20033-20044. DOI: https://doi.org/10.1074/jbc.M909008199, PMID: 10748113

Wenzel HJ, Cole TB, Born DE, Schwartzkroin PA, Palmiter RD. 1997. Ultrastructural localization of zinc transporter-3 (ZnT-3) to synaptic vesicle membranes within mossy fiber boutons in the hippocampus of mouse and monkey. *PNAS* **94**:12676-12681. DOI: https://doi.org/10.1073/pnas.94.23.12676, PMID: 9356509